OBSERVATIONS OF STRUCTURES IN THE INNER COMA OF CHIRON WITH THE *HST* PLANETARY CAMERA[1]

KAREN J. MEECH
University of Hawaii, Honolulu, Hawaii 96822
Electronic mail: meech@ifa.hawaii.edu

MARC W. BUIE
Lowell Observatory, Flagstaff, Arizona 86001
Electronic mail: buie@lowell.edu

NALIN H. SAMARASINHA, BEATRICE E. A. MUELLER, AND MICHAEL J. S. BELTON
National Optical Astronomy Observatories, Tucson, Arizona 85719
Electronic mail: {nalin, muller, belton}@noao.edu

Received 1996 May 19; revised 1996 November 13

ABSTRACT

We have obtained a series of images of 2060 Chiron with the *HST* Planetary Camera on 3 nights near its minimum geocentric distance in 1993 ($\Delta=8.342$ AU). Extended structure was visible within a radial distance of 0.3″ from the nucleus. We interpret the structure to be the bound ballistic atmosphere and exopause boundary (at $R_e \approx 1800$ km) hypothesized by Meech & Belton [AJ, 100, 1323 (1990)]. Near simultaneous ground-based photometry of the outer coma showed a steep surface brightness profile with a logarithmic gradient of -3.1 ± 0.03 (from 1–3.3″) and -2.2 ± 0.01 (from 3.3–9.8″). The inner gradient is consistent with the *HST* observations. The color of the outer coma from the ground-based data is neutral at short wavelengths, and slightly redder than the sun at the longer wavelengths. The outer coma scatters neutrally at much shorter wavelengths than most comets, which suggests that the outer coma is populated by smaller grains ($\lambda \leq 0.6\mu$m). Combining the grain size of particles escaping into the outer coma with the *HST* observations, and constraints on grain densities, we infer that the density of Chiron is relatively low, near $\rho_{Nuc} < 10^3$ kg m^{-3}. Within the exopause boundary the nucleus contributes approximately 80% of the total light. © *1997 American Astronomical Society.* [S0004-6256(97)03202-0]

1. INTRODUCTION

Chiron is a member of the growing inventory of known unusual outer solar system objects which may be representatives of bodies from the Kuiper belt. During its 1996 perihelion passage, Chiron has been the target of an intense observational campaign in order to understand its activity, which has been unusual both in the level of activity at large heliocentric distances, r, and the type of activity which it has exhibited. One of the long-standing questions about Chiron concerns the size of the nucleus. A variety of observations have shown that Chiron is large for a comet. Because of its unusually large mass due to its size, it is likely that gravity plays a role in the structure and development of the coma. The first size estimate from Lebofsky *et al.* (1984) suggested a diameter of $180+40/-50$ km. Later estimates by Spencer *et al.* (1989) with improved thermal models gave an upper limit near 400 km for the diameter. A combination of improved thermal models and *IRAS* observations lead Sykes & Walker (1991) to suggest an upper limit of 372 km. Jewitt & Luu (1992) also obtained an upper limit from a non-detection in the sub-mm, which yielded a diameter upper limit of 300 km. More recently, Buie *et al.* (1993) and Bus *et al.* (1996) observed an occultation of Chiron which yielded a diameter ≥ 180 km. In addition, Campins *et al.* (1994) have detected Chiron at 10 and 20 μm on 5 different dates in 1991, 1993, and 1994, and have estimated the diameter to be near 182 km. Finally, observations of the occultation of Ch08 by Elliot *et al.* (1995) suggest a 3σ upper limit to Chiron's radius of 156 km. For the purposes of this paper, we assume therefore that the radius of Chiron lies between $90 < R_N$ [km] < 150.

Chiron's large size, thus its large inferred mass, almost certainly exerts a gravitational influence on the coma structure. Meech & Belton (1990) used a heuristic approach to try to understand what the effect of the stronger gravity on Chiron might be on the observable aspects of its activity and coma. Chiron's activity has been characterized by long, slow outbursts at extreme distances from the sun at $r=17$ and $r=13$ AU (Bus *et al.* 1991; Hartman *et al.* 1990). The model of Meech & Belton asserted that the long-lived outbursts

[1]Based on observations with the NASA/ESA *Hubble Space Telescope* obtained at the Space Telescope Science Institute, which is operated by the Association of Universities for Research in Astronomy, Incorporated, under NASA contract NAS5-26555, and on observations made at the National Optical Astronomy Observatories, operated by the Association of Universities for Research in Astronomy, Inc., under contract with the National Science Foundation.

 0004-6256/97/113(2)/844/19/$10.00

could be explained by a bound ballistic coma which slowly decayed after the cessation of intermittent activity. The coma was populated by particles on sub-orbital trajectories which could become perturbed by radiation pressure and have residence times of months in the atmosphere. In this model, the observable coma represents those particles which were small enough to escape the gravity of Chiron. After the grains decouple from the gas flow a few nuclear radii, R_N, from Chiron's surface, the distance scales of interest in this model include the Hill radius, R_H, which is the distance at which solar gravitational acceleration on the dust begins to dominate over the gravity from Chiron (c.f. Tanaka & Ida 1996, and references therein), and the exopause boundary, R_e [km]. This distance, which is the distance at which the radiation pressure acceleration exceeds the gravity of the nucleus, is given by

$$R_e = r[M_N/(M_\odot \beta)]^{1/2}, \quad (1)$$

where r [km] is the heliocentric distance, $M_N = 4\pi R_N^3 \rho_N/3$ [kg] is the nucleus mass for a nuclear density of ρ_N [kg m^{-3}] and size R_N [m], and $M_\odot$ [kg] is the solar mass. Here β is the ratio of the solar radiation pressure acceleration on the grain to the solar gravity and is given by:

$$\beta = kQ_{\rm pr}/(\rho_{\rm gr} a_{\rm gr}), \quad (2)$$

where $k = 5.7398 \times 10^{-4}$ kg m^{-2}, $Q_{\rm pr}$ is the radiation pressure scattering efficiency, $\rho_{\rm gr}$ [kg m^{-3}] is the grain density, and $a_{\rm gr}$ [m] is the grain radius. In contrast to the situation for Chiron, most comets near the sun have a Hill radius and exopause which lie close to the nucleus, within the zone where the dust is strongly coupled to the gas outflow, and therefore for these comets the nucleus gravity has little effect on the coma morphology. Using the development above, the model of Meech & Belton (1990) was able to successfully model the lightcurve behavior from 1977 through 1992 as the result of sublimation from 1 or 2 regions rich in CO, roughly 1–2 km in size.

Luu & Jewitt (1990) have argued against the possibility of a gravitationally bound coma on the basis that the inner bound coma cannot be a photometrically important entity. They base this on a comparison of Chiron's coma profiles with model star profiles they constructed (brightness versus radius) which had varying amounts of coma. The coma was considered to be unbound, and represented by a power law, and was convolved with the estimated seeing to compare with observations. From the best match of these models to the data, they determined what the brightness contribution of the nucleus plus any bound, unresolved coma contribution could be. Comparing this to their estimate of the nucleus brightness alone, they concluded that the bound coma could not contribute more than 10%–20% of the light within 1″ from the nucleus during 1990 January and was therefore not photometrically important (and hence could not account for the long, slow outbursts). Stern *et al.* (1993), on the other hand, argued that the bound coma should not exist based on numerical simulations of the lifetimes of grains in orbit. They found that particles do not tend to enter the quasi-stable orbits proposed by Meech & Belton, having short orbital lifetimes, typically on the order of days, rather than months. Their models, however, neglected the rotation of Chiron on the initial injection velocity into the coma and had only a simplified simulation of particulate injection conditions. While their calculations showed that it is likely that only a small fraction of the injected particles will end up in long lifetime ballistic orbits, it is clear that the inclusion of rotation and specific locations of active areas into the model can extend the lifetimes of many of the particles and that the balance between the fluxes of escaping and ballistically trapped particles can be changed in favor of the latter component (c.f. Banaszkiewicz & Ip 1991). We are presently investigating these effects in detailed model calculations.

Unfortunately, the bound portion of the coma for all reasonable nucleus sizes, particle size distributions, and nucleus densities, is predicted to be below the limit of resolution from the ground, and thus the debate is not easily settled. In an attempt to resolve this question we used the *Hubble Space Telescope* (*HST*) Planetary Camera (pre-COSTAR) to obtain a series of images of 2060 Chiron. The goal was to use Chiron's radial brightness distribution (i) to locate an exopause structure which would indicate gravitational control by the nucleus over the structure of the inner coma, and (ii) to explore the inner coma for indications of active regions which could reveal the number and location of major sources on the nucleus. The exopause boundary, which is determined both by the mass of Chiron and the particle scattering efficiencies, was expected to be between 0.3–0.8″ from Chiron (2,000–5,000 km) for grain sizes near 1 μm (near 0.1–0.2″ for 0.1 μm grains and 1–2.5″ for 10 μm grains) when Chiron was at its 1993 minimum geocentric distance ($\Delta = 8.342$ AU on 1993 February 14). The light we receive from Chiron has contributions from 3 sources: (i) the nucleus, which is not quite resolved and thus effectively a point source; (ii) the unbound coma of small dust grains (typically < 1 μm in size; with a surface brightness profile with a power law with an index < -2); and (iii) from the possible gravitationally bound dust atmosphere which we expect may be approximated over a limited range by a power law. The expected signature of the exopause, or boundary of this dust atmosphere, was to have been manifested as a change in power law slope of the surface brightness distribution of Chiron's coma.

2. OBSERVATIONS AND DATA REDUCTIONS

2.1 HST Data

HST observations of Chiron were made with the Planetary Camera (platescale: 0.0439″ pixel^{-1}) on 1993 February 22 and 23, and on 1993 March 8. On each of the dates in February, 18 images of 120 sec each were obtained, and in March eight 120 sec images were obtained, for a total integration of 5,280 sec. All of the observations were obtained with the F555W filter, which roughly corresponds to the m_V bandpass. This filter was selected because it had the best *HST* calibration frames. The journal of observations is presented in Table 1, and the geometric circumstances are shown in Table 2. Because of the severe spherical aberration present in the *HST* primary (Burrows *et al.*, 1991) and be-

TABLE 1. Log of Chiron and PSF observations.

Frame[a]		Object	UT	Exp	Frame		Object	UT	Exp
1993 February 22 (w1a7510)					cs28	at	Chiron	05:08:18	120.0
					cs29	bt	Chiron	05:16:18	120.0
cs01	1t	Chiron	01:56:18	120.0	cs30	ct	Chiron	05:27:18	120.0
cs02	2t	Chiron	02:04:18	120.0	cs31	dt	Chiron	05:35:18	120.0
cs03	3t	Chiron	02:12:18	120.0					
					cs32	et	Chiron	06:45:18	120.0
cs04	4t	Chiron	03:26:18	120.0	cs33	ft	Chiron	06:53:18	120.0
cs05	5t	Chiron	03:34:18	120.0	cs34	gt	Chiron	07:04:18	120.0
cs06	6t	Chiron	03:45:18	120.0	cs35	ht	Chiron	07:12:18	120.0
cs07	7t	Chiron	03:53:18	120.0	cs36	it	Chiron	07:20:18	120.0
cs08	8t	Chiron	05:02:18	120.0	**1993 February 23** (w1a7530)				
cs09	9t	Chiron	05:10:18	120.0					
cs10	at	Chiron	05:21:18	120.0	ps01	1t	HD946160	19:50:18	0.3
cs11	bt	Chiron	05:29:18	120.0	ps02	2t	HD946160	19:56:18	0.3
					ps03	3t	HD946160	20:04:18	0.3
cs12	ct	Chiron	06:38:18	120.0	ps04	4t	HD946160	20:10:18	0.3
cs13	dt	Chiron	06:46:18	120.0					
cs14	et	Chiron	06:58:18	120.0	**1993 March 8** (w1a7040)				
cs15	ft	Chiron	07:06:18	120.0					
					cs37	1t	Chiron	08:17:18	120.0
cs16	gt	Chiron	08:15:18	120.0	cs38	2t	Chiron	08:25:18	120.0
cs17	ht	Chiron	08:23:18	120.0					
cs18	it	Chiron	08:31:18	120.0	cs39	3t	Chiron	09:43:18	120.0
					cs40	4t	Chiron	09:51:18	120.0
1993 February 23 (w1a7020)					cs41	5t	Chiron	10:02:18	120.0
					cs42	6t	Chiron	10:10:18	120.0
cs19	1t	Chiron	01:55:18	120.0					
cs20	2t	Chiron	02:03:18	120.0	cs43	7t	Chiron	11:19:18	120.0
cs21	3t	Chiron	02:11:18	120.0	cs44	8t	Chiron	11:27:18	120.0
cs22	4t	Chiron	02:22:18	120.0					
cs23	5t	Chiron	02:30:18	120.0	**1993 March 9** (w1a7050)				
cs24	6t	Chiron	03:32:18	120.0	ps05	1t	HD946160	13:15:18	0.3
cs25	7t	Chiron	03:40:18	120.0	ps06	2t	HD946160	13:21:18	0.3
cs26	8t	Chiron	03:51:18	120.0	ps07	3t	HD946160	13:27:18	0.3
cs27	9t	Chiron	03:59:18	120.0	ps08	4t	HD946160	13:33:18	0.3

Notes to TABLE 1.

[a]The second frame number is the last 2 digits of the original STScI archival file name appended to the prefixes which are in parentheses after the dates. Images are organized by orbital groups; exposure times are in seconds.

cause of the variation of the PSF with wavelength and position on the CCD, and our need to accurately deconvolve the Chiron images in order to search for coma very close to the core of the image, additional observations of a point spread function star, HD 946160, were made on 1993 February 23 and March 9. The position of the PSF star was within ≈ 20 pixels of the location of Chiron (i.e., about 1″) at the optimum pointing for PC6 during the February observations, and was more ideally located in March, only 10 pixels ($\approx 0.5''$) from the Chiron position. A detailed comparison of the PSFs in the two positions showed significant differencesin the low surface brightness tendril structure between Chiron and the February PSFs, as well as a difference in the scale (this is a strong function of position on the CCD), therefore only the March PSF observations were used in the deconvolution of the data as discussed below. The observations were obtained in the coarse lock mode, with jitter as determined from the spacecraft telemetry to have a magnitude of less than 0.6 pixels for the Chiron images. This estimate of the jitter was convolved with the PSF images to test

TABLE 2. Geometric circumstances.

UT Date	r [AU]	Δ [AU]	Phase [degree]	Pixel size [km]	1 arcsec [km]
1993 Feb 19	9.311	8.345	1.33	1324.6	6048.4
1993 Feb 20	9.309	8.347	1.31	1324.9	6049.9
1993 Feb 22	9.307	8.351	1.64	265.7	6052.8
1993 Feb 23	9.306	8.353	1.74	265.8	6054.2
1993 Mar 08	9.287	8.412	3.04	267.7	6097.0

for its effect on the deconvolution process. The gain for the detector was 7.5e$^-$/ADU, with a read noise of 13e$^-$.

The data were reprocessed through the standard STScI pipeline processing programs combined with the best known calibration files as of 1994 February. The normal cosmic ray cleaning routines in IRAF and in the STSDAS packages were not well-suited to cleaning the images because of the sharpness of the central peak of Chiron, which was inevitably treated as a cosmic ray. Instead we used an unsharp masking procedure to reduce the steep surface brightness gradients in the central part of the images to identify cosmic rays and form an image mask for each image which consisted of uniform values of 1 everywhere except for regions containing cosmic rays which were set to large negative values (typically 10^3 times the sigma of the background). The masks were then multiplied by the images and any pixels which met the rejection criterion were replaced by a cubic spline fit to their neighbors. Our technique explicitly excluded removal of cosmic rays in the inner core (diameter 16 pixels) of the images, because the sharpness of the image peak may allow it to be mistaken for a cosmic ray. Based on the expected cosmic ray rate for the CCD it is possible that there were some faint events in the inner core which were not corrected, but as shown later, this does not appear to have affected the deconvolutions. Because our technique did not rigorously consider the noise characteristics of the data, we compared these results with a cr-rejection technique which used the WFPC.COMBINE task as described by Shaw & Horne (1992). Using this task, we combined images based on noise parameters determined from our data. When we compared the results from this task with the same images combined after using our previous method, there were significant deviations in the peak Chiron counts. This was an artifact of the WFPC.COMBINE routine which was a result of the slight differences in Chiron's placement on the CCD (tracking jitter). When Chiron's image was well-centered on a pixel the peak counts were high compared to frames where the core light fell on 2 or more pixels, and in these high count frames Chiron's core was erroneously treated as a cosmic ray and removed.

Finally, to prepare the images for deconvolution, all were registered using the image maxima, after background subtraction and were stacked. Images have been stacked by orbital groups which are separated in Table 1, in order to more easily look for variations with time. At the wavelength of our observations the PSF core is undersampled. However, because of spacecraft jitter, we are limited in our ability to resolve the innermost core, so that we did not require use of an interpolation scheme to register the images. Because we are interested only in the innermost region near Chiron's nucleus, we extracted small sub-arrays (191 × 191 pixels, corresponding to 8.4″ on a side) from the PC images to speed up the computations.

2.2 Ground-Based Data

Deep coma images were obtained of Chiron nearly simultaneous with the *HST* observations using the UH 2.2 m telescope with a 2048 pixel^2 CCD on 1993 February 19 and 20. The data were obtained under photometric conditions in a dark sky (new moon was on February 20; sky brightness was m_R=21.1 mag arcsec^{-2}) with moderate seeing conditions (0.8–0.9″). Calibrations were obtained using observations of standards from Landolt (1983, 1992). The purpose of the ground-based observations was to assess the extent of Chiron's outer coma and the coma color in order to make comparisons with the *HST* data and make inferences about the sizes of the particles escaping from the inner coma based on the color of the coma. All of the images were guided at sidereal rates, and the exposures were kept short (60 sec) so that Chiron would not trail. The data were reduced using standard techniques, and then were co-added to form the composite images shown in Fig. 1. Measurements of the centroids of a large number of field stars were used to compute the best telescope guiding offsets between the images in order to create a composite image tracked at sidereal rate. After these offsets were applied to each image, the ephemeris rates for Chiron were used with the CCD plate scale (0.219″ pix^{-1}) to compute the final offsets to create the composite image tracked on Chiron as shown in Fig. 1. In these images, Chiron's dust extends ≈15″ (9×10^4 km) to the NW as projected on the plane of the sky.

In addition to the deep coma images, we also obtained frequent measurements of Chiron's color during 20 nights in the period 1993 January 26–1993 March 17 using the Lowell 42-inch and 72-inch telescopes and the Kitt Peak National Observatory 2.1 m telescope. The purpose of the monitoring was (i) to look for outburst activity which might be associated with any features detected in the inner coma from *HST*, and (ii) to monitor Chiron's overall brightness so we could constrain the amount of coma contribution in the inner core. A composite lightcurve of the ground-based data from previously published data (Bus *et al.* 1991; Hartman *et al.* 1990; Meech & Belton 1990, and unpublished data from our observing campaign) is shown in Fig. 2. The reduced magnitude, H_V, is plotted versus heliocentric distance. For clarity, we have plotted only nightly averages. The *HST* observations were obtained while Chiron was mid-way between its "quiescent" and brightest periods. A full discussion of the new unpublished data (which comprises over 100 nights of data from 1986 to the present) will be provided in a future paper (Meech *et al.* 1993b, and in preparation). During this period, the average Chiron colors were: $m_B-m_V=0.619\pm0.006$, $m_V-m_R=0.371\pm0.006$, and $m_R-m_I=0.375\pm0.006$ (within a 5″ radius circular aperture).

3. ANALYSIS

3.1 Image Deconvolution

There are currently several deconvolution techniques which are in use for the analysis of pre-COSTAR *HST* images. Among these include the Richardson-Lucy and Maximum Entropy techniques. The Richardson-Lucy technique has had proven success with the *HST* data and is the most widely used technique for its deconvolution. It is particularly appropriate because it converges to the maximum likelihood for Poisson statistics (e.g., appropriate for optical data). However, the drawback with this technique is that it is not always clear when the iterations should be stopped, and pre-

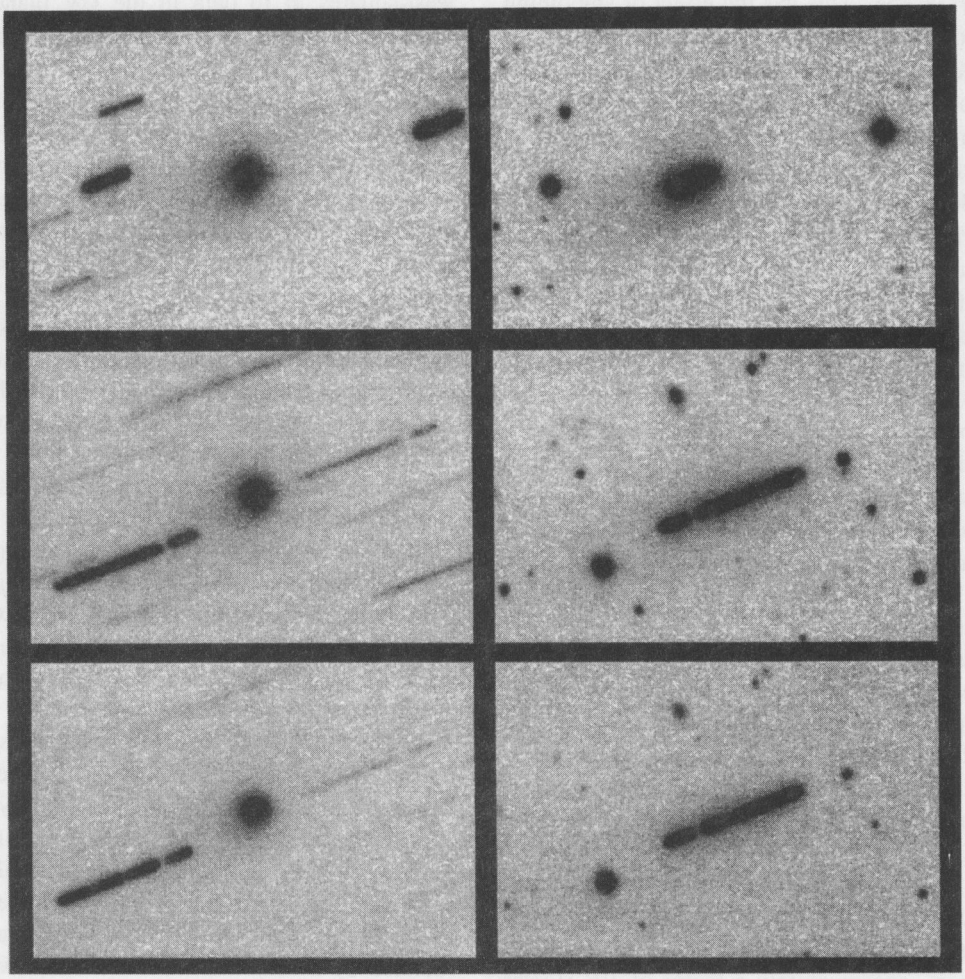

FIG. 1. Ground-based images of Chiron obtained with the UH 2.2 m telescope close to the time of the *HST* observations. The left-hand column shows composite images stacked and co-added to simulate Chiron's motion and the right-hand column represents the same images co-added at sidereal rates in order to compare the stellar profiles with that of Chiron. The top images are from 1993 February 19 at 07:30:12 UT (midtime) with a total exposure time of 1260 seconds through the m_R filter. The middle images are a 1980 sec total exposure from 1993 February 20 at 08:27:53 UT (midtime) through the m_R filter, and the bottom images are a 1800 sec total exposure through the m_B filter (08:26:47 UT midtime). In all frames N is at the bottom and E is at the right, and the field of view corresponds to 1.8 × 1.2 arcmin.

mature cessation of iterations can lead to loss of photometric accuracy. On the other hand, while the Maximum Entropy techniques can sometimes produce better results, they are not always stable, and can be difficult to use.

Instead, we have elected to employ the σ-CLEAN routine (Högbom 1974; Keel 1991) used in two-dimensional aperture synthesis image reconstruction to remove the effects of the telescope aberrations. With this technique it is assumed that the intensity of the object is comprised of the sum of δ-functions. The observed PSF images serve as a "dirty" model or beam and the Chiron images become the "dirty" observations. The CLEAN algorithm finds the peak of the absolute value of the data in the dirty image and subtracts from this the observed PSF multiplied by γP, where P is the peak value found in the image, and γ is the gain, to produce a residual image. At the same time the true object image is built up by adding a δ-function of the intensity at the peak multiplied by the gain times the sum of the normalized PSF to the output image at the (x,y) location of the peak. In this manner the technique is flux-preserving. The process is iterated until peaks are being found near the threshold of the sky background. For this procedure, we used a stacked sky-subtracted PSF which had been normalized to a peak value of 1, which goes to zero at the edges of the array. The final image is then convolved with a true model PSF which is represented by a Gaussian, in order to simulate the "beam"

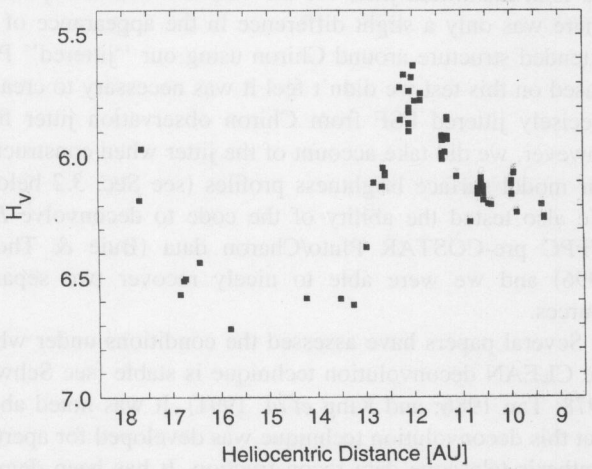

FIG. 2. Chiron lightcurve reduced to $r=1$, $\Delta=1$, $\alpha=0$ vs heliocentric distance. Only nightly averages have been plotted for clarity.

or non-aberrated *HST* PSF. This has the effect of smoothing the data and restoring an estimate of the unaberrated PSF (see Keel 1991; King *et al.* 1991; this is similar to using an apodizing mask to suppress the side lobes in an Airy diffraction pattern). From Keel (1991), experience shows that for the *HST* WFC data, the optimal Gaussian should have $\sigma=1.5$ pixels (0.065″), which is roughly the diffraction limit of the telescope. For the cleaning procedure we used a 61 × 61 pixel box centered on the maximum of the stacked PSF, and a box of 45 × 45 pixels centered on Chiron. The PSF sub-array was larger to allow it to wander around to find the peak in the Chiron images. The initial CLEAN iterations were done with $\gamma=0.05$.

The CLEAN packages were initially developed for synthetic aperture radar (Högbom 1974), where the noise characteristics are fundamentally different than for the optical *HST* images. According to Keel (1991), the noise variations in the optical may be higher in regions of higher surface brightness which can lead to a condition of noise locking which will produce pairs of closely spaced positive and negative components. His solution to this problem was to modify the CLEAN algorithm to search for the most statistically significant peak in the data, rather than the extrema. In our application of the CLEAN routine written for IDL (the Interactive Data Language; Research Systems, Inc.), we employed both a standard peak-finding algorithm to locate the maximum as well as a cross correlation of the PSF with the image to find the most significant peak. In order to speed up the cross correlation, we ran the cross correlation on a $2n+1$ box centered on the PSF. For $n=10$, each iteration took roughly 54 sec—approximately a factor of 10^3 slower than the simple peak-finding algorithm. Both methods were tested with $\gamma=0.1$, and 5000 iterations, and they produced the same results. Since the cross correlation method took significantly longer to run, after initial tests we used only the standard peak finding algorithm.

As a test of our routine, we cleaned one of our stacked PSFs against the other and were able to recover a point source. Additionally, we created an approximation of a jittered PSF (since the PSF exposures were shorter than the Chiron frames by a factor of 600) by convolving it with a Gaussian of half width of 0.6 pix, which was our estimate of the total maximum jitter for the 120 sec Chiron exposures. There was only a slight difference in the appearance of the extended structure around Chiron using our "jittered" PSF. Based on this test we didn't feel it was necessary to create a precisely jittered PSF from Chiron observation jitter files, however, we did take account of the jitter when constructing our model surface brightness profiles (see Sec. *3.2* below). We also tested the ability of the code to deconvolve *HST* WFPC pre-COSTAR Pluto/Charon data (Buie & Tholen 1996) and we were able to nicely recover two separate sources.

Several papers have assessed the conditions under which the CLEAN deconvolution technique is stable (see Schwarz 1978; Tan 1986; and King *et al.* 1991). It was noted above that this deconvolution technique was developed for aperture synthesis telescope data reconstruction. It has been demonstrated that this deconvolution technique is analogous to a least-squares fit to data in the UV plane (Fourier space). Schwarz (1978) showed that while there always exists a solution, there may be many solutions. In cases of a simple point source on a blank sky, the correct solution is likely to be found first, however, when there is extended emission, or the noise characteristics found in optical data, other solutions may be found unless care is taken to select the proper gain and to stop the iterations before they go too far. Tan (1986) has shown that although the image deconvolution can depend on the loop gain values, by selecting a small loop gain, and by stopping the iterations once the residuals did not decrease consistently, that divergence from a good solution could be controlled. Small loop gains also ameliorate the well-known difficulty of CLEAN to recover significant extended structure (i.e., with large gains a "fringing" effect appears in the deconvolved data). The present Chiron data is well-suited to the CLEAN deconvolution in that we have a high S/N point source with only a small amount of extended emission. After a series of tests, with gains ranging from 0.01–0.1 and iterations from 10^3–10^5, we found that 10^4 iterations (requiring $\approx$10 min per image) and $\gamma=0.08$ worked well for the S/N of our data and the *HST* noise characteristics.

For completeness, we also ran some tests on our composite *HST* image with the new generation Richardson-Lucy image restoration technique (the Hook-Lucy implementation). We ran a series of deconvolutions ranging from 5 to 100 iterations. While all the results were similar (except for the smallest iterations), the best result of the tests was around 40 iterations, and this produced a point-source like core surrounded by a very faint halo. The halo was more extended than the material seen in the σ-CLEAN deconvolutions, and residual tendril structure from the PSF was evident, showing that the Richardson-Lucy technique did not provide as satisfactory results.

Based on this, we selected the σ-CLEAN method as being optimal for our data set. Our initial deconvolutions were done with respect to orbital groups (as listed in Table 1) to search for time variations, however, because of the low signal to noise of the low surface-brightness coma in the restored images, we present only composite deconvolutions from the stacked images 1–44 (i.e., from all 3 visits) in the following discussion. In Fig. 3 we present a comparison of the unrestored *HST* composite image (upper left), the composite PSF image (upper right) and the restored images using the σ-CLEAN and Richardson-Lucy techniques (lower left and right, respectively). The effect of jitter which smoothes out some of the fine structure in the longer Chiron images compared to the PSF image, can be seen as a difference in feature sharpness in the top images in Fig. 3. The σ-CLEAN restoration shows low surface brightness material close to the core, which we interpret to be the inner coma that is discussed below. This feature was not visible when we applied the same techniques to the other stacked PSF star, nor in our tests of other point-sources.

3.2 Surface Brightness Profiles and Normalization

To look at the extent and distribution of material in Chiron's coma, surface brightness profiles (SB versus r) for the

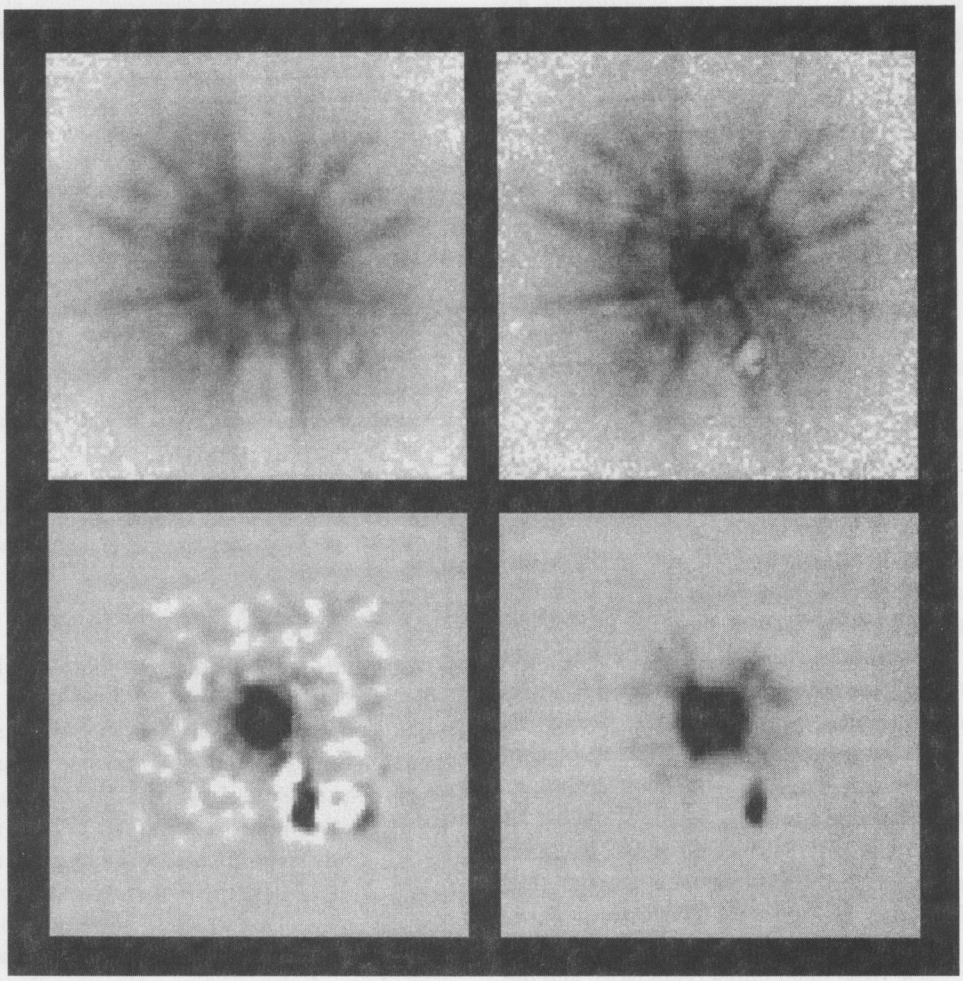

FIG. 3. Raw image of all of the stacked Chiron data (total exposure 5280 sec; upper left), the raw PSF stacked image from March (upper right), the Chiron data deconvolved with the σ-CLEAN technique (lower left) and the Richardson-Lucy algorithm (lower right). Each image is 100×100 pixels^2, or 4.4″ on a side. The measle or CCD blemish which was close to the optimum pointing position of *HST* is evident in the image. As discussed in the text, it did not adversely effect the image restorations.

images were computed in IDL using a routine which computes the average counts per pixel in an annulus centered on the image centroid. The routine accurately takes account of the fractional area of a pixel which lies within the annulus (c.f. Buie & Bus 1992 for an extensive discussion of the software). The profiles in this paper were computed with an annulus width $dr=0.5$ pixels such that the central annulus counts exactly matched the counts in the peak pixel. This allows the comparison of 2 profiles by normalizing to the counts in the peak pixel.

In order to assess how far out to believe the surface brightness profiles, something especially critical with the *HST* data and our interpretation of the extended material visible in the reconstructed images, we need to accurately account for the noise contributions in the profiles. This includes photon noise from the source, the sky noise and the readnoise. The error associated with the counts in an annulus is

$$\sigma^2_{\rm Tot}=gC+(gA\sigma_{\rm sky})^2+\sigma^2_{\rm RN}, \quad (3)$$

where C is the measured sky-subtracted counts [ADU] for Chiron, g is the gain [e^- ADU^{-1}], A is the area of the annulus, and $\sigma_{\rm RN}$ is the readnoise. Although the sky background, which will be our dominant noise source in the coma limiting detection, has been subtracted off in the *HST* images before deconvolution, we can determine the average sky and the sigma of the mean on the sky background using a large area on the CCD outside the region where there is coma to get good statistics. For our data, $\sigma_{\rm sky}=1.5$ cnts pix^{-1}, where $\sigma_{\rm sky}=\sigma/N^{0.5}$ and $\sigma=$ variance$^{0.5}$ of the sky background, and N is the number of sky pixels used in computing the background. The resulting error bars on the *HST* profiles suggest that the skynoise dominates beyond 0.6–0.7″ (14–16 pix) from the core, and that we can reliably only interpret the data within this distance–about 4,000 km from the nucleus.

The logarithmic brightness gradient given by

$$m_{sb}=d\ln(B)/d\ln(p), \quad (4)$$

where B is the brightness of the coma and p'' is the projected distance in from the center. The brightness gradient is expected to be equal to -1 for a steady-state unbound coma. Previous measurements of the outer coma of Chiron have all been steeper than this (Meech & Belton 1990; Luu & Jewitt 1990; and West 1991), ranging between -1.5 and -2.6. The steeper slopes up to -1.5 have been interpreted as phase angle and radiation pressure effects, and slopes steeper than

this have been suggested as evidence for sublimating icy grains (see discussion in Sec *5.3* below). These gradients are determined from the radial surface brightness profiles by noting that $\ln(B) = -0.921034(SB)$.

The ground-based data from 1993 February 20 may be fit by $m_{sb} = -2.25 \pm 0.4$ between $p = 1$–$9.8''$; however, the profile is best fit by 2 slopes: $m_{sb} = -3.10 \pm 0.03$ for $p = 1$–$3.3''$ and $m_{sb} = -2.2 \pm 0.01$ for $p = 3.3$–$9.8''$.

3.3 Simulations

The complete recovery of an unblurred image by deconvolution can never be achieved, therefore it is important to test the effects of the deconvolution with models (Lauer *et al.* 1992a, 1992b). We therefore developed model Chiron images which were convolved with the *HST* stacked PSF. Using these simulations, we were able to compare the results of the deconvolved simulations to the "truth" in the simulations and ascertain whether or not the procedure was able to restore the images, whether it was creating any artifacts in the process, and what our sensitivity would be to detect changes in the slope of the coma gradient indicative of an exopause boundary. The heuristic model images we developed consisted of three components. The first was a constant surface brightness nucleus of size R_N, with a surface brightness, SB_{Nuc}, which contributes a user-specified fraction of the total light inside a particular projected radial distance, $p = p_{Nuc}$. The coma consists of two components, both represented by power law light distributions. The inner coma is represented by a p^{α_1} surface brightness distribution, SB_{inner}, inside $p_{inner} = R_e$ (the inner coma boundary), and the outer coma is represented by a p^{α_2} surface brightness distribution, SB_{outer}, with the inner coma-outer coma boundary being continuous. The total surface brightness, SB, of the coma is then given by

$$\begin{aligned} SB &= SB_{Nuc} + 0.5 SB_{inner} p^{\alpha_1}, && p < p_{Nuc}, \\ SB &= SB_{inner} p^{\alpha_1}, && p_{Nuc} < p < p_{inner}, \\ SB &= SB_{outer} p^{\alpha_2}, && p > p_{inner}. \end{aligned} \quad (5)$$

The factor of 0.5 is present because there is no contribution from the far side coma in the innermost region. By adding the total flux from the nucleus to the contribution from the coma, we can express the constants SB_{inner} and SB_{outer} in terms of the known parameters:

$$\begin{aligned} SB_{inner} &= [(f_{Nuc}^{-1} - 1) p_{Nuc}^2 SB_{Nuc}(\alpha_1 + 2)] / \\ &\quad [2p_{inner}^{(\alpha_1+2)} - p_{Nuc}^{(\alpha_1+2)}], \\ SB_{outer} &= SB_{inner} p_{inner}^{(\alpha_1 - \alpha_2)}, \end{aligned} \quad (6)$$

where f_{Nuc} is the fraction of the total light contributed by the nucleus within $p = p_{inner}$.

Prior to creating simulated images for comparison with the deconvolved *HST* data, we were able to place some constraints on the model parameters. The lower limit to features which may be detected is given by the telescope diffraction limit (1.4 pixels = 0.061″ at $\lambda = 5555$ Å), which corresponds to ≈370 km at the comet. If the exopause were much larger than 0.5″ (≈3,000 km) then it would be detectable from the ground, thus we constrain the exopause boundary between $370 < R_e$ [km] < 3000. For the inner coma surface brightness profile power-law index, a canonical steady-state coma should give -1 (based on an inverse square law dependence on particle density), however, for a bound atmosphere, the density drops more steeply than that of a power law (i.e., exponentially) for distances beyond 1 atmospheric scale height. Thus, unless the particles are fragmenting, it is likely that the inner coma gradient slope would be $\alpha_1 < -1$. The outer coma gradient slope is constrained to match the ground-based observations closest to the *HST* observations, and should be near $\alpha_2 = -3$ (see Sec. *3.2* above). Finally, by definition, absolute limits to the fraction of the total light, f, which is contributed by the nucleus must be $0 < f < 1$. Ground-based observations place more stringent constraints on f, and suggest that it is a variable quantity, depending on Chiron's activity. Meech & Belton (1990) found a coma contribution, f_{coma}, to the total light between 0.45–0.56 for a 5″ aperture, and Luu & Jewitt (1990) inferred a coma contribution less than 0.2. Likewise, Campins *et al.* (1994) suggested that the total coma contribution was 0.3. West (1991) found that the coma contribution was 0.44 in a 5.6″ aperture for the m_V filter. The implied $f = 1 - f_{coma}$ for these observations is $0.44 < f < 0.8$. For the *HST* data we are parameterizing the data in terms of f_{Nuc}, which is the fractional nucleus contribution inside p_{inner}, i.e., at a much smaller effective aperture, and the fraction of the total light contributed by the nucleus should be even larger than the ground-based limits, especially since from the ground-based observations we see that the total brightness of Chiron was not excessively bright at this time (i.e., there was not a disproportionately large contribution from the coma; see Fig. 2). We will take $f_{Nuc} > 0.5$ to be a hard limit for the simulations.

We created a suite of 220 images with a range of parameters as shown in Table 3. The models were created to have the same signal-to-noise as the stacked *HST* images. Figure 4 shows logarithmic surface brightness profiles of the simulations at various stages in the processing discussed below, so that the effects of each of the steps may be clearly discerned.

TABLE 3. Chiron simulations—range in parameters.

α_1 [1]	α_2 [2]	R_e [3]	f_{Nuc} [4]
−0.5	−1	600	0.001
−0.75	−1.5	900	0.1
−1.0	−1.9	1200	0.2
−1.5	−2.0	1500	0.3
−1.7	−2.5	1800	0.4
−1.9	−2.57	2100	0.5
−2.3	−3.0	2400	0.6
−2.5	−3.25	3000	0.7
−3.0	−3.5		0.8
−3.5	−4.0		0.9
−4.0	−4.5		0.999
−4.5			

Notes to TABLE 3.

[1]Inner coma surface brightness power law index; [2]outer coma surface brightness power law index; [3]exopause boundary [km] i.e., boundary between inner and outer coma; [4]fraction of the total flux which is contributed by the nucleus within R_e.

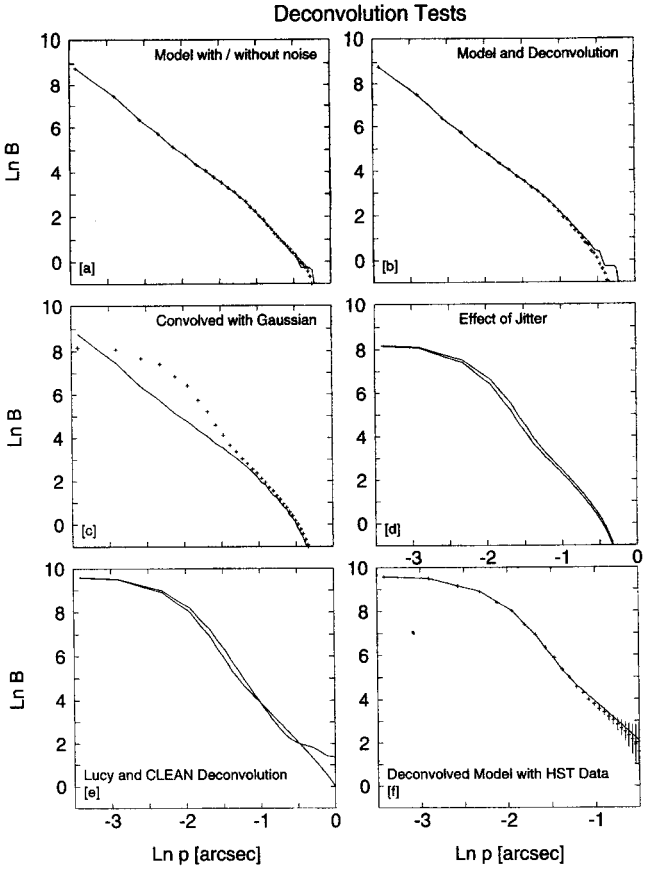

FIG. 4. Illustration of the model simulations and deconvolution tests and sequential effects on data, using a best-fit model: $R_N = 90$ km, $\alpha_1 = -2.45$, $\alpha_2 = -3.25$, $R_e = 1800$ km, $f_{Nuc} = 0.1$. Logarithmic surface brightness profiles for simulated Chiron image (a) with (+) and without noise (solid line); (b) simulation with noise convolved with *HST* PSF (solid line) and deconvolved using the CLEAN algorithm (+); (c) deconvolved simulation (solid line) and comparison after convolution with gaussian with $\sigma = 1.5$ pix (+) to restore the original *HST* PSF (see Sec. *3.1*); (d) effect of jitter on the deconvolved data (top curve includes jitter, bottom curve does not); (e) comparison of the profiles using the Lucy (top curve at $\ln(p) = -2$) and CLEAN deconvolutions (Note: normalizations are different from a–d); and (f) comparison of final deconvolved simulation with jitter (solid curve) with the deconvolved *HST* stacked Chiron data (+). The brightness is in arbitrary units. Error bars have been suppressed for all simulations for clarity; however the formal errors have been computed and plotted for the *HST* data in panel (f).

To each of these simulated images we added poisson noise, with the same characteristics expected from the real *HST* data [$g = 7.5$ e$^-$/ADU, $\sigma_{RN} = 13$e$^-$; see Fig. 4(a)]. The simulations were convolved with our scaled stacked PSF (using the IRAF routine IMCONV), and then the images were reconstructed using our σ-CLEAN algorithm (Fig. 4(b)). The restored simulations were then convolved with a Gaussian with $\sigma = 1.5$ pixels to restore the original *HST* PSF (Fig. 4(c); refer to discussion in Sec *3.1*). This step has a significant effect on the shape of the logarithmic surface brightness profile, so that it is no longer approximated by a straight line segment; however, the range of simulations we ran allowed us to examine the sensitivity we would have to changes in parameters such as the exopause distance and differences between the power laws α_1 and α_2. To assess the effect that telescope jitter had on the images, they were convolved with a Gaussian of $\sigma = 0.6$ pixels to simulate the smearing caused by jitter in the long object exposures (as compared to the PSF exposures). The effect of the jitter shown in Fig. 4(d), while small, was essential to achieving a reasonable match to the observations with any set of parameters. Figure 4(e) compares the results for the σ-CLEAN and the Richardson-Lucy techniques, and showing that for the present data set the σ-CLEAN method produced significantly better results. In the final panel we compare the best-fit simulation with the logarithmic surface brightness profile for the stacked, deconvolved *HST* data.

The ability of the σ-CLEAN algorithm to reconstruct the images is shown in Fig. 5 which is a comparison of the *HST* Chiron data (center column) with simulated images at various processing stages. Our best fit Chiron plus coma model is shown in the left column and a non-resolved nucleus without coma is shown in the right-hand column. The top row represents simulations with noise and jitter added; the images in the middle row have been convolved with the *HST* PSF (i.e., they are as they would appear imaged through the *HST*), and the bottom row is after deconvolution and Gaussian smoothing. Comparison of the top and bottom rows shows our inability to recover detail which exceeds the diffraction limit of the telescope and is the reason the point source appears broadened. Structure which is present beyond this limit is recoverable, however. A comparison of the images on the bottom row shows that Chiron (center) clearly has extended structure which is similar in appearance to the structure in the image at bottom left. As will be shown below, this is most consistent with the signature expected from a 2-component coma model for the exopause structure. It should be noted that the measle did not significantly affect the deconvolution of the images. The most pronounced effect is that it creates a noise spike in the logarithmic surface brightness profile near $\ln(p) = +0.5$, however since at this distance from Chiron the sky background errors are rapidly increasing, we do not even consider this region in our analysis.

While it is clear from Fig. 5 that there is extended structure around the reconstructed Chiron image, we cannot ascertain the nature of the structure without testing our sensitivity to detecting changes in the free parameters throughout the reconstruction process. Figure 6 shows the logarithmic surface brightness profiles for sets of simulations which tested the sensitivity of each of the free parameters. In each panel, the *HST* data are plotted with pluses and the models are shown as solid lines. The parameters which were held fixed are shown in the lower left of each panel with the range of free parameters shown at the center bottom. We present logarithmic surface brightness plots rather than surface brightness profiles, because the affects of the changing parameters are more readily apparent in these plots. We found in general that the nucleus size had little apparent effect on the logarithmic surface brightness profile (other than the correlation between nucleus size and exopause boundary). The parameter f_{Nuc} did not significantly change the shape of the logarithmic surface brightness profile until $f_{Nuc} > 0.9$, and up until this point, a smaller value lead to a higher curve. The outer coma power law index, α_2, was likewise easy to interpret as this affected only the portion of the curve outside

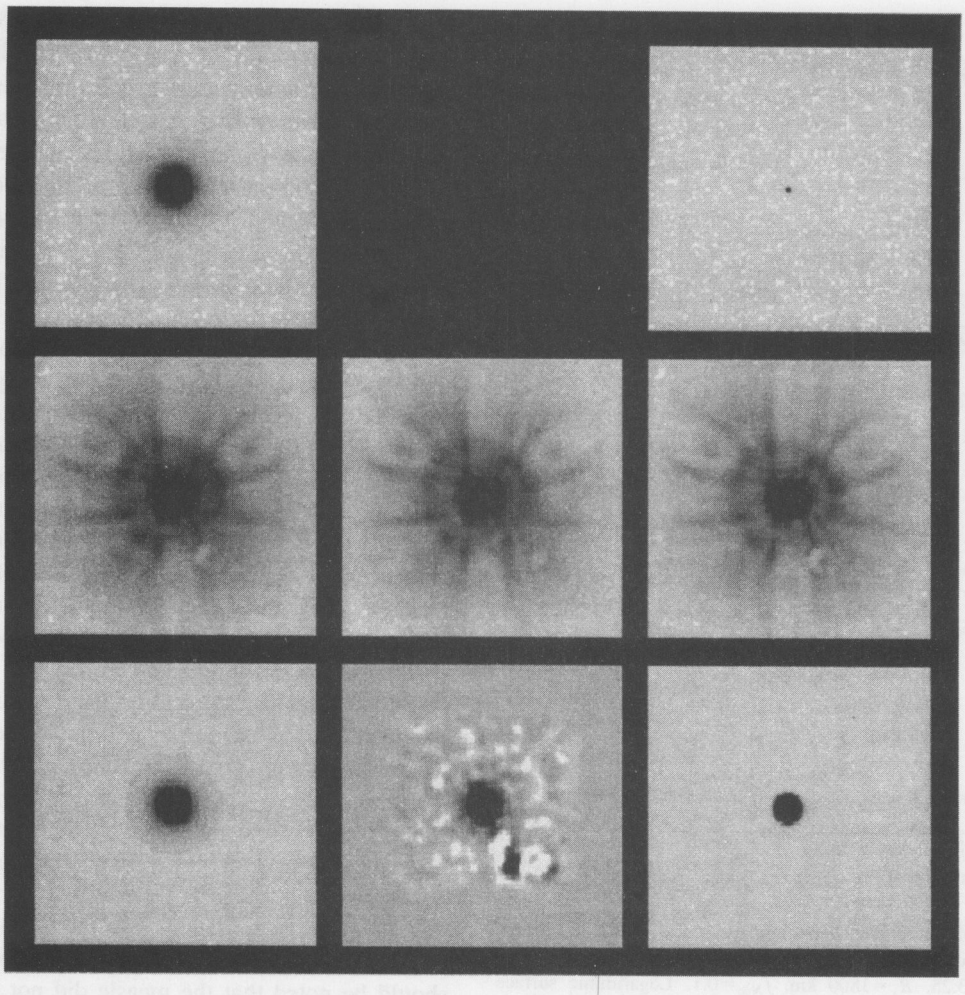

FIG. 5. Comparison of simulated images at various processing stages with the *HST* Chiron data. The left column is for the best-fit Chiron simulation shown in Fig. 4, which consists of a 2-component coma, and the right column represents a simulated stellar point source which has been processed in the same manner. The central column is the *HST* Chiron data. The top row represents the simulation with noise and jitter added; the middle row is after the data have been convolved with the *HST* PSF, and the bottom row is after the deconvolution process and gaussian smoothing (e.g., beam restoration).

R_e, and it was quite easy to distinguish changes as small as 0.1 in this parameter. The inner coma power index, α_1, had the most profound affect on the profiles, changing both the shape and the magnitude of the values in the curve. Likewise changing distance of the exopause boundary did not produce a straightforward change in the profile, as this change is interrelated with other parameters. The simulations could easily distinguish the change in slope which marked the exopause boundary for all reasonable distances expected for Chiron (from $R_e = 600$–3000 km) *provided* that the difference in power laws between the inner and outer comae was greater than about 0.5.

In order to eliminate the possibility that the extended structure seen near Chiron in Figs. 3 and 5 was the manifestation of the high surface brightness portion of a typical single-component coma, we ran simulations where we kept the values α_1 and α_2 equal. This is shown in parts (a) and (b) of Fig. 7. A reasonable fit is produced with a single-component coma model in panel (a), however, the fit required an unreasonably low f_{Nuc} (near 0.1) which is not supported by other observations (as listed above). Given that the total brightness of Chiron as seen in Fig. 2 did not indicate that there could have been an extraordinary amount of coma at the time of the *HST* observations compared to past ground-based observations from which the estimates of f were made, this indicates that Chiron is not dominated by the dust coma as panel (a) would suggest. The best single-component fit with a more reasonable nucleus fraction, $f_{Nuc} = 0.8$, is shown in Fig. 7(b), and is clearly a poor fit to the data. In contrast, the best fits with the 2-component model are shown in Figs. 7(c) and 7(d). Again disallowing the fit shown in Fig. 7(c) because of the small f_{Nuc}, we find that the best fit to the *HST* observations is found with a 2-component coma, with $R_e \approx 1800$ km, $\alpha_1 = -1.7$ and $\alpha_2 = -3.5$, which is in agreement with the observed ground-based data for the outer coma. The fit is not perfect, especially near $\ln(p) = -1.5$ to -2.0, however, we expect that our heuristic model is an over-simplification of the true coma dynamics. The important point to note, however, is that the single-component models cannot be made to fit the *HST* Chiron data.

The final result of the comparison of the *HST* data with the deconvolved simulations is that the best fits require a 2-component coma, with a $R_e \approx 1800 \pm 200$ km. The error on the exopause distance is the value by how much the distance can change and be corrected for by changes in the other

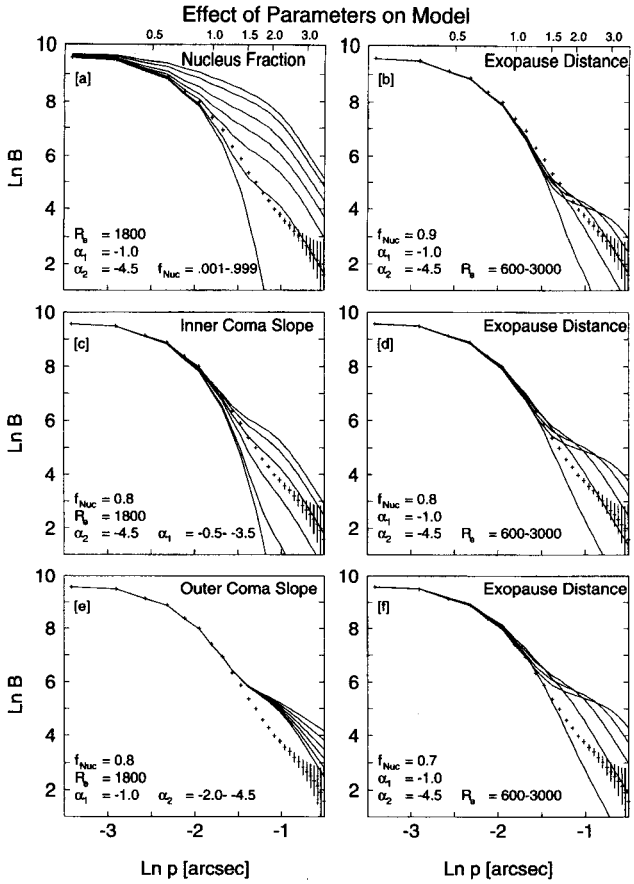

FIG. 6. Effect of the free parameters on the model logarithmic surface brightness profiles, a comparison between models (solid curves) and deconvolved *HST* data (crosses). For each figure, the parameters which are held constant are listed at the lower left, where α_1 is the inner coma exponent, α_2 is the outer coma exponent, R_e is the exopause distance, and f_{Nuc} is the fraction of the total light in the peak pixel which is contributed by the nucleus within $p_{inner}=R_e$. The scale in 10^3 km is listed at the top of the figures. (a) Variation of fraction of light contributed by nucleus. From the upper curve to the lowest curve, $f_{Nuc}=0.001$, 0.1, 0.3, 0.5, 0.7, 0.9, and 0.999 (top to bottom). (b) Variation of exopause distance, with R_e varying from 600, 1200, 1800, 2400, and 3000 km (left to right; where the curves are well-separated). (c) Variation of inner coma slope from -0.5, -1.0, -1.5, -2.0, -2.5, -3.0, -3.5 (top curve to bottom), (d) Same as (b), but with a different nucleus fraction; (e) Variation of outer coma slope from -2.0, -2.5, -3.0, -3.5, -4.0, -4.5 (top to bottom curves); and (f) Same as (b), but with a different nucleus fraction. The brightness is in arbitrary units. Note that the pixel scale may be determined from the spacing of the (+) symbols which are plotted at intervals of 0.5 pixel. Total plotted region is 0.6″ (13.5 pix) from the core of the Chiron images.

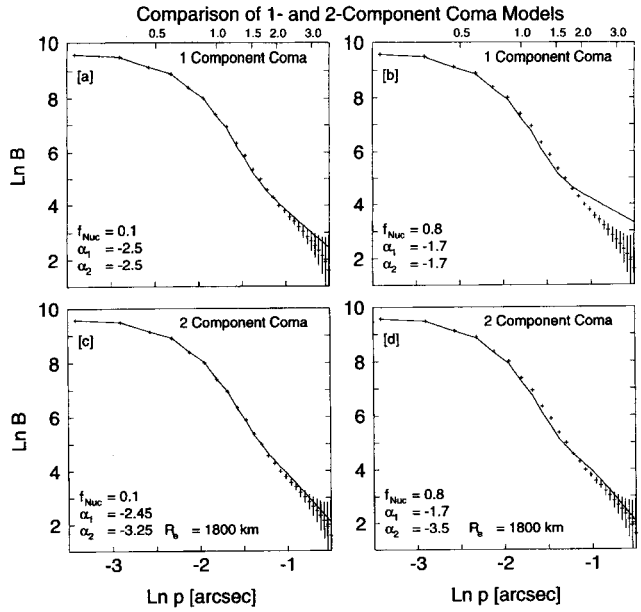

FIG. 7. Comparison of the logarithmic surface brightness profiles of the best-fit models for the single component coma (a, b) and the two-component coma (c, d). Frames (a) and (c) show the best fits, which require $f_{Nuc}=0.1$, and frames (b) and (d) show the best fits with the more realistic $f_{Nuc}=0.8$. The model parameters are noted in the lower left of each frame. The brightness is in arbitrary units. The scale in 10^3 km is listed at the top of the figures.

parameters. If R_e varies by more than this, the fit becomes noticeably worse. However, it should be noted that this assumes a fit to a model which is certainly more simplified than the actual situation at Chiron.

4. ABSOLUTE CALIBRATION

A direct comparison of the *HST* Chiron fluxes with the UH 2.2 m ground-based observations requires absolute calibration for the *HST* data. Using the information from Sparks *et al.* (1993), and from the photometric keywords in the *HST* headers, we derived a magnitude $m_{F555W}=16.00$ for Chiron on 1993 February 22 (this was the magnitude obtained within a 1″ aperture which is the radius at which the data are dominated by sky noise). There is a non-negligible color-dependent transformation between the m_{F555W} and the m_V filter (Harris *et al.* 1991). Using the m_B-m_V color as determined from the ground, we find $m_V=m_{F555W}+0.04=16.04$. The total magnitude within a 5″ aperture from the ground was $m_V=16.33$ on 1993 February 20. It is unlikely that Chiron's brightness changed by over 30% during the time between the MKO and *HST* observations, so we conclude that comparisons between the ground and space fluxes from Chiron are only accurate to about 30%. This is consistent with statements made in the *HST* Data Handbook from 1995 which suggests that calibration accuracies between 3%–30% are typical. It should be noted that these observations were taken roughly 8 months after the last decontamination (Ritchie & MacKenty 1993), which can affect the calibration by up to 15%. This discrepancy cannot be accounted for by the rotational variation which has a maximum range of 0.088 mag (Bus *et al.* 1989). Given these difficulties, we did not attempt to make direct flux comparisons between the *HST* and ground-based data. The surface brightness profile of the composite Chiron images from Mauna Kea from 1993 February 20 is shown in Fig. 8, along with the corresponding logarithmic surface brightness profile. The MKO and *HST* profiles have been arbitrarily shifted to form a smooth curve for comparison. It is clear from the figure that the strength of the ground-based observations is for the low-surface brightness observations and that the *HST* is superior for resolution.

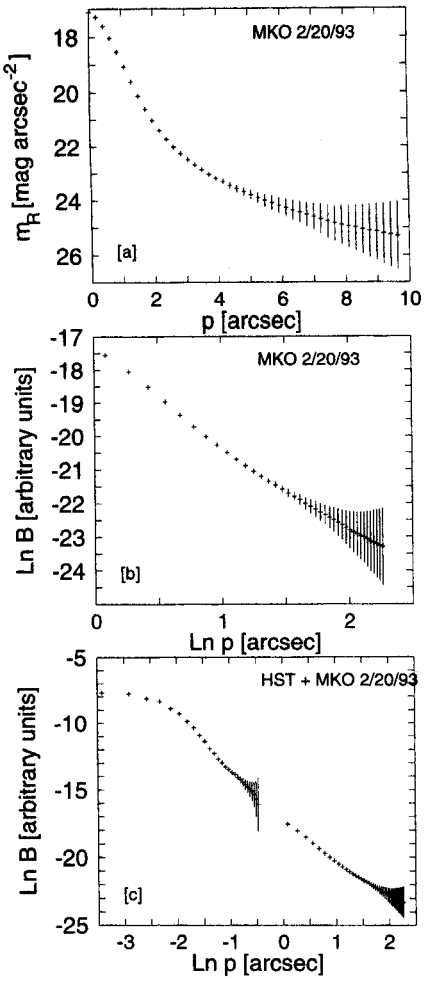

FIG. 8. (a) Surface brightness profile in m_R [mag arcsec^{-2}] of Chiron vs radius [arcsec] for ground-based data obtained from the Mauna Kea (MKO) 2.2 m telescope on 2/20/93. (b) Logarithmic surface brightness profile for MKO data. Data for $p<1''$ has been excluded because it is affected by the seeing; and (c) logarithmic surface brightness profile for the ground-based and *HST* data combined.

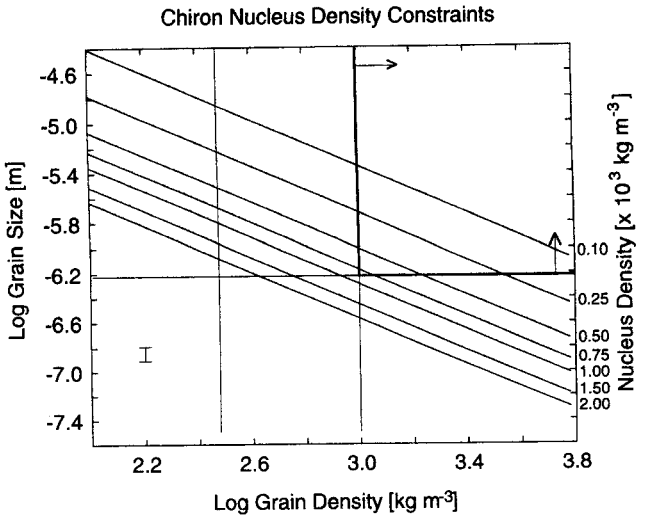

FIG. 9. Nucleus density contours (diagonal lines) plotted on a graph of grain size vs grain density. The vertical lines represent likely lower limits for IDP grain densities, and the horizontal line represents a likely lower limit to grain sizes trapped in the inner coma based on measured colors of Chiron's outer coma. The most likely phase space for the density of Chiron lies to the right of the grain density limits and above the grain size limit (as shown by the heavy lines and arrows). The diagonal nucleus density lines are computed from the *HST* exopause location measurement. For reference, a representative error bar for the constant c (as described in the text) is shown. This is the amount that the nucleus density contours might move vertically in the plot.

5. DISCUSSION

5.1 Interpretation of the Exopause Size

As was discussed earlier in Sec. 1, the extent of the exopause is controlled by the nucleus gravity (i.e., the mass, M_N) and the effect of radiation pressure acceleration on the grains, as parametrized by β. In order to assess the plausibility of the small exopause radius implying a low nucleus density, we need to carefully examine the extent to which we know several of the parameters which control the size of the exopause. We can re-write Eq. (1) in terms of the nuclear density, ρ_N [kg m^{-3}], the coma dust grain density, ρ_{gr} [kg m^{-3}], and the coma mean dust grain size, a_{gr} [m]:

$$\log(a_{gr}) = c - \log(\rho_N) - \log(\rho_{gr}), \tag{7}$$

where

$$c = \log[3M_\odot k Q_{pr}(R_e^2/R_N^3)/4\pi r^2] \tag{8}$$

and

$$\sigma_c = [(0.869\sigma_{R_e}/R_e)^2 + (1.303\sigma_{R_N}/R_N)^2]^{1/2}. \tag{9}$$

The term c is a constant equal to -0.21 ± 0.12 for Chiron at the time of the *HST* observations, for $Q_{pr}\approx 1$. We have assumed an exopause distance of $R_e = 1800\pm200$ km as our best fit, with the error being determined by the resolution at which we can detect changes in the fits. We are using the nucleus radius of $R_N = 90\pm5$ km as being the best estimate of the radius (Bus *et al.* 1996; Campins *et al.* 1994; Lebofsky *et al.* 1984). The error on the exopause radius, σ_{R_e}, has roughly a factor of 2 larger contribution to the overall error in c, than does σ_{R_N} with the current parameters, so by more accurately measuring c, we can more accurately constrain our nucleus density estimates. Figure 9 shows the phase space for grain size and grain density with contours of nucleus density appropriate for the *HST* Chiron measurements. The issue is to determine which regions in the figure, if any, are excluded, and to see if there are plausible conditions under which a nucleus with a density near that of water-ice would be permitted. The error on the constant c, above, is the amount by which the nucleus density contours might shift in the vertical direction.

To place constraints on the coma particle sizes, we can examine the coma colors which have been observed as a function of heliocentric distance and time. Particles which are small compared to the wavelength of radiation will be in the Rayleigh scattering regime, and the scattered radiation will appear blue. As was shown by Jewitt & Meech (1986), the reflectivity gradients, S', as a function of wavelength for a collection of comets at different heliocentric distances indicated that neutral scattering occurs near $\lambda\approx 2$ μm, suggesting that the optically dominant mean particle size in most cometary comae is around 2 μm. P/Halley observations summarized by Lamy *et al.* (1989) showed the same trend. The

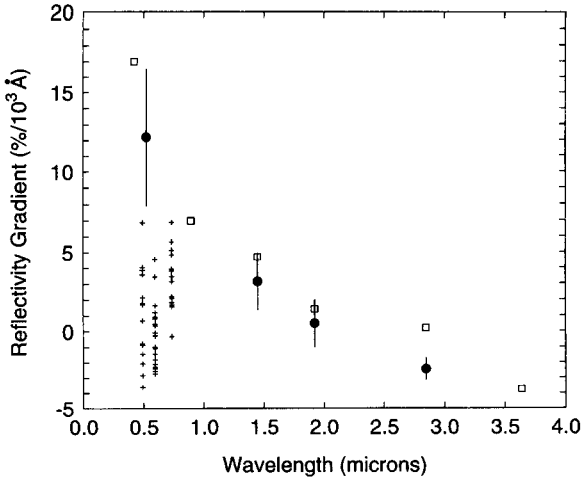

FIG. 10. Reflectivity gradient (% per 10^3 Å) vs wavelength for a selection of comets (filled circles; Jewitt & Meech 1986), for P/Halley (open squares; Lamy *et al.* 1989), and for Chiron (+; unpublished). The figure suggests that neutral scattering for Chiron's outer coma occurs at much smaller grain sizes ($\lambda \approx 0.6$ μm) than for typical comets ($\lambda \approx 2$ μm).

reflectivity gradients for Chiron expressed in $\%/10^3$ are calculated from

$$S'(\%/10^3 \text{ Å}) = (20/\Delta\lambda)[10^{(0.4\Delta m)} - 1]/[10^{0.4\Delta m} + 1], \quad (10)$$

where Δm is the comet color minus the solar color and $\Delta\lambda$ (μm) is the difference in the effective wavelengths of the bandpasses. The Chiron reflectivity gradients calculated using data from Meech *et al.* (in preparation) are presented in Fig. 10 in comparison with the data from Jewitt & Meech (1986) and Lamy *et al.* (1989). The figure shows that the dust in Chiron's coma scatters neutrally ($S' = 0$) at much shorter wavelengths (near $\lambda \approx 0.6$ μm) than most comets and further shows considerable variability. Figure 11 plots S' versus heliocentric distance for 3 colors in comparison with Chiron's activity level as indicated by the changes in H_V. The trends in the $m_V - m_R$ and $m_R - m_I$ colors suggest a correlation of reddening with outburst activity, in particular near 11.4 AU. The single measurement of a $m_B - m_V$ reflectivity gradient near $r = 16$ AU when Chiron was with minimal, if any activity, may be more representative of the surface materials on Chiron, suggesting the bluer colors may be the result of particle size effects in the outer coma which is observed from the ground. In this case, the interpretation we can draw from these figures is that typically, the larger particles are trapped in the inner coma, and the coma color, which is dominated by the outer coma is neutral due to the presence of smaller grains. During an outburst, there is sufficient energy to eject larger particles into the outer coma. Both these considerations and the neutral scattering in general at these wavelengths suggests that the cutoff in particle size for those grains escaping into the outer coma is near $a_{gr} = \lambda \approx 0.6$ μm.

The 0.6 μm limit for grains escaping into the coma is drawn as a horizontal line in Fig. 9 ($\log(a_{gr}) = -6.22$). The region below the line is excluded for possible nucleus densities since for these nucleus densities and grain density/size combinations the very small particles which we *do* see in the coma based on the coma color evidence would be trapped within the exopause by Chiron's gravity.

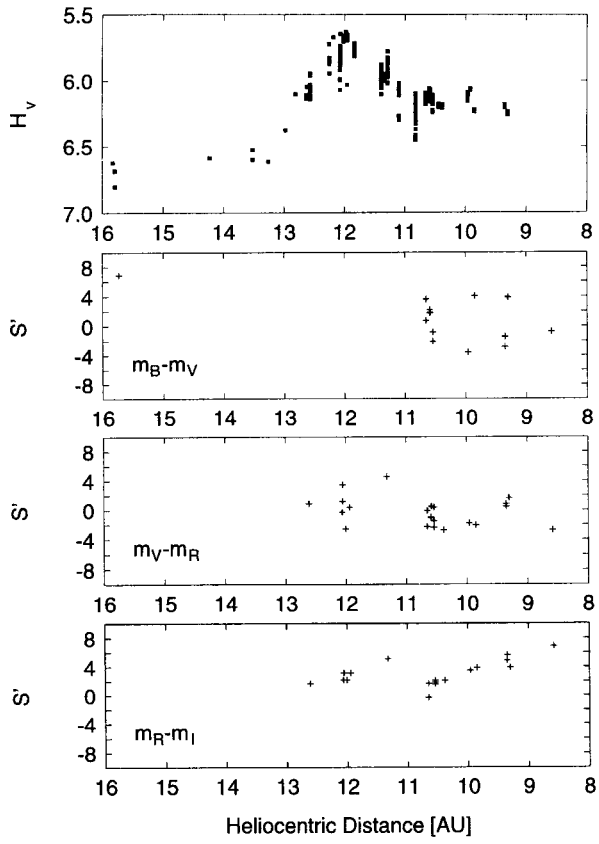

FIG. 11. Reflectivity gradient for Chiron vs heliocentric distance for the $m_B - m_V$, $m_V - m_R$ and $m_R - m_I$ filters in comparison to the general activity level as indicated by H_V (top panel). Instead of the nightly averages plotted in Fig. 2, the top panel plots all of the data, as an indication of the bursty nature of Chiron's activity.

There is less direct evidence which may be used to constrain the possible range of coma grain densities in Fig. 9. The best analogues to the coma grains are the interplanetary dust particles (IDPs) which have been collected in the Earth's upper atmosphere (Bradley & Brownlee 1986). According to Bradley *et al.*, (1988), the IDPs are a mineralogically diverse group which fall into 2 broad classes: the anhydrous particles (which contain pyroxenes and olivines and are fairly porous) and the layer lattice silicates (which are more compact). In addition, there is also a carbonaceous component to the IDPs. These particles as a group are similar to the chondritic meteorites, although are probably more representative of early grain-forming reactions. Although it should be cautioned that the IDPs collected in this manner may be more representative of material from asteroids, since particles on asteroidal orbits are more likely to survive Earth atmospheric entry, many investigations (e.g., Hanner 1988; Gehrz & Hanner 1988; Walker 1988; Bradley *et al.* 1988) have concluded that the Comet P/Halley spectra are consistent with those of IDPs if the models include a mixture of IDP particle types.

The IDP particles have been observed to have bulk densities ranging between $0.7\text{–}3.0 \times 10^3$ kg m^{-3} (Bradley *et al.* 1988; Brownlee *et al.* 1980; Weiss-Wrana 1983). Whereas

TABLE 4. Densities and optical constants for cometary dust candidate materials.

Material	Density [kg $m^{-3} \times 10^3$]	Index of Refraction n	k	Comments
silicate	2.2	1.4–1.7	0.03	consistent with Halley spectra
olivine	3.3	1.66	1.0×10^{-4}	
carbon				
graphite	5.2	2.7	1.4	
disordered		1.88	0.77	vitreous carbon
magnetite	2.16	2.56	0.6	present in meteorites
chondrite	2.2	1.90	0.019	general similarities to IDPs
tholin	1.45	1.56–1.67	0.002–0.04	Sometimes referred to as dirty silicates.
		1.68	0.04	

the compacted densities for the IDP materials (silicates, carbon, magnetite, chondrites) may range only from about 2–5 $\times 10^3$ kg m^{-3}, as shown in Table 4, the porosity of the IDPs varies considerably from near zero to over 50%. It has been found that about 25% of the particles are quite porous, yielding lower bulk densities. The optical constants for the various measured IDP compositions are also listed in Table 4 (from Lamy *et al.* 1987; Khare *et al.* 1987; Hanner 1988). At the time of the P/Halley apparition, there was considerable effort devoted to modeling the scattering from the coma particles in order to interpret the observed phase curves and the polarization curves. The average abundances for the Comet Halley dust as measured from Giotto were chondritic, with a carbon enrichment over chondrites. In addition, organic CHON components were also detected (Kissel *et al.* 1986). Lamy *et al.* (1987) were able to use Mie scattering to model the observations and found that the data were compatible with a mixture of rough moderately absorbing silicate grains if the grain density decreased with increasing radius, which is the expected behavior of fractal aggregates (Donn & Meakin 1987). The Mie models also showed that the best fit to the polarization data required mixture of particle types similar to IDPs which included moderately absorbing rough silicate grains (Lamy *et al.* 1987; Brooke *et al.* 1987) with the addition of some organics (Mukai *et al.* 1987). Mukai *et al.* found that the P/Halley coma dust was best represented with material having the index of refraction of $m = 1.38 - 0.04i$ in the visible region ($\lambda = 0.365$–0.73 μm). This is in agreement with the modelling of the Zodiacal light scattering which also shows that a mixture of particles consistent with IDPs are required to reproduce the observations (Lamy & Perrin 1980; Weiss-Wrana 1983). The optical constants for cometary dust candidate materials are also summarized in Table 4.

Additionally, there were several reported direct measurements of grain density in P/Halley's coma using particle penetration through thin films on the Vega and Giotto dust detectors. Smirnov *et al.* (1987) and Krasnopolsky *et al.* (1987) estimated that the particle densities were near 10^3 kg m^{-3} in the inner coma and considerably less in the outer coma. This may have been the result of fragmentation of the large highly porous fractal aggregates. Similarly, Pailer & Grün (1980) found that approximately 30% of the micrometeoroids detected by the Helios experiment had densities lower than 10^3 kg m^{-3}.

Given the good match between the IDP scattering properties and the fits to the grains in the coma of P/Halley and other comets using a mixture of IDP grains and organic components we propose that $\rho_{gr} > 10^3$ kg m^{-3} is probably a reasonable "most probable" lower bound for the grain densities for Fig. 9. The large porosity in the IDPs (up to 50%), may in part be due to sublimation of some volatile materials (e.g., water) from the pore spaces, which is not likely to occur at the distance of Chiron. Experiments with sublimation of volatile laden water-ice (e.g., CO and CO_2, CH_4 and N_2) have shown that the effect of the more volatile materials within the water ice is the ejection of water-ice grains as the highly volatile gases are released at different temperatures (Bar-Nun *et al.* 1985; Bar-Nun & Kleinfeld 1989). This implies that the high porosity of the IDPs might be an upper limit to the porosity of Chiron's dust grains for Chiron since while IDP interstitial ices may have sublimated the temperatures were too low for water-ice sublimation at Chiron's distance. In addition, the least dense grains in Halley's coma were found in the outer coma, and in the case of Chiron, we are most interested in the inner coma conditions. Based upon these arguments, the vertical line at $\log(\rho_{gr}) = 3.0$ represents the most likely lower grain density limit for Chiron's coma grains, although it would not be impossible to find grains of densities down to near $\log(\rho_{gr}) = 2.48$ (0.3×10^3 kg m^{-3}) as shown by the vertical line at the left.

From these arguments, it is clear from Fig. 9, that the *most likely* interpretation of the observed exopause distance is that the density of Chiron's nucleus is low, $\rho_N < 10^3$ kg m^{-3} and that it might require extreme circumstances to interpret the data in terms of a canonical water-ice nucleus with a bulk density higher than 10^3 kg m^{-3}. Propagating the errors in our constant c, which governs the placement of the density contours in the figure, gives an uncertainty of the nucleus density of around $\sigma_{\rho_N} \approx 280$ kg m^{-3} assuming $\rho_{gr} = 10^3$ kg m^{-3} and $a_{gr} = 0.6$ μm.

Our constraints here are not extremely tight for several reasons. The accuracy to which we know c, depends on the

TABLE 5. Cometary material strength estimates.

Tensile Strength [Nt m^{-2}]	Type	Reference	Technique
$\approx 10^3$		Mendis *et al.* 1985	tidal stress; sungrazer Ikeya-Seki ($\rho = 1.0$)
4.3×10^2		Mendis *et al.* 1985	tidal stresses on Brooks 2 at perijove ($\rho = 1.0$)
10^3	mantle	Möhlmann 1995	icy dirtball nucleus models
10^2–10^3		Boehnhardt & Fechtig 1987	electrostatic fragmentation of P/Halley dust as measured from Giotto
10^2–10^4		Hughes 1991	analysis of cometary spin & size characteristics
10^4		Sekanina 1982	ram pressure from outgassing from nucleus
10^8		Mendis *et al.* 1985	shock strength during Tunguska breakup
		Sekanina 1983	
10^8		Green 1989	survival of sungrazers–for non-porous ice
10^3–10^5		Boehnhardt & Fechtig 1987	laboratory measurements of artificial nuclei
3.5×10^5	porous ice	Möhlmann 1995	icy dirtball nucleus models
2×10^2–10^3	dry snow	Möhlmann 1995	icy dirtball nucleus models
10^4–10^6	porous snow	Green 1989	50% porous snow
$(1$–$5) \times 10^3$	meteoroids	Sekanina 1985	fragmentation ram pressure, Draconids
	IDPs	Bradley & Brownlee 1986	analysis of interplanetary dust particles
6×10^6–4×10^8	chondrites	Wasson 1974	measurements of chondrites
4×10^8	iron	Wasson 1974	measurements of iron meteorites

realistic scattering properties of cometary dust which is incorporated in the term Q_{pr}. Burns *et al.* (1979) performed a series of calculations of the radiation pressure efficiency for spherical grains and found that the value was typically around 1. For more realistic non-spherical particles, the scattered radiation is redistributed from the forward direction to a more isotropic pattern because of multiple scattering. Since Q_{pr} is a combination of the scattering and absorption efficiencies and the scattering efficiency is slightly larger for rough particles, it is expected that Q_{pr} should be slightly larger than 1. The only situation where $Q_{pr} \geqslant 2$ is for metallic particles which have very different optical properties than the dirty dielectric cometary dust candidates in Table 4. Finally, since our optically dominant grains in the coma have wavelengths slightly longer than where the peak scattering efficiency occurs (near $\lambda = 0.4$ μm for dirty dielectrics), we conclude that $Q_{pr} \approx 1$ is a reasonable assumption. Finally, because the image quality of the *HST* observations is such that there is a significant error on the position of the nucleus density contours in Fig. 9, we conclude that new *HST* observations combined with better ground-based monitoring for a detailed analysis of the grain scattering properties and sizes, should significantly improve our nucleus density constraints.

5.2 Low-Density Implications

It is important to assess whether a representative bulk density as low as 0.5–1×10^3 kg m^{-3} is realistic given the large size of the nucleus or whether there would be significant compression at the core. A crude estimate of the central pressures inside Chiron assuming $R_N = 90$ km and assuming that the density is constant with depth inside the nucleus may be made from the following relation derived from the equation of hydrostatic equilibrium

$$P_{cent} = 2\pi G \rho_N^2 R_N^2 / 3 \tag{11}$$

where $G = 6.67 \times 10^{-11}$ Nt m^2 kg^{-2} is the gravitational constant. This gives $P_{cent} = 2.8 - 11.3 \times 10^5$ Nt m^{-2} (which is 2.8–11.3 atmospheres = 2.8–11.3 bar). The Murnaghan equation of state (Murnagan 1967), as derived from an application of hydrostatic pressure to an unstressed solid in the approximation of low pressure, may be used to approximate the ratio of the central density to the uncompressed density ρ_0:

$$\rho_{cent}/\rho_0 = (P_{cent} B/K + 1)^{1/B} \tag{12}$$

where K is the bulk modulus (i.e., the stiffness or incompressibility), and the pressure derivative of the bulk modulus, $B = [\partial K/\partial P] \approx 3.3$–$4$ for most materials. We have used values from Green (1989) to estimate $K = 10^8$–10^{10} for porous cometary ice. Using these values, the ratio, ρ_{cent}/ρ_0, remains small—between 1.00003 and 1.01. Thus, the assumption of constant density inside a body this small is reasonable.

Table 5 lists published estimates and constraints on the tensile strengths of the cometary material, two meteorite types and snow for comparison. There is a wide range in the strength values, with the weakest values being significantly lower than the estimate of Chiron's central pressure for our lower density estimates. Given the recent studies of comet D/Shoemaker-Levy 9 (D/1993 F2 = D/SL9) and new models of comet formation, however, it is plausible that Chiron can have a bulk density as low as $\rho_N = 500$ kg m^{-3} with a radius of 90 km, yet have sufficient strength in the interior. The models of Asphaug & Benz (1994) for the tidal disruption of D/SL9 indicated that the best representation of the nucleus was as a strengthless aggregate or rubble pile of cometesimals which were held together gravitationally, and which had a bulk density of 500 kg m^{-3}. The idea of the cometary rubble pile was first proposed by Weissman (1986) and Donn & Hughes (1986) and is now considered to be a likely result for cometary accretion models (Weidenschilling 1994). According to Weidenshilling's work, grains which are settling to the solar nebula mid-plane are unable to achieve high enough densities for the layer to fragment into gravitationally bound condensations because of the effect that radial pressure gradients in nebular gas and the coupling of grains and gas has on inducing turbulence. Instead, the grains will undergo collisional accretion until they are large enough to decouple from the gas; this occurs at estimated sizes of 10's

TABLE 6. Evolution of cometary nucleus density estimates.

Nucleus Density [kg $m^{-3} \times 10^3$]	Reference	Technique
0.28–0.65	Rickman 1989	H_2O outgassing and non-gravitational analysis on Halley
0.03–4.9	Peale 1989	H_2O outgassing and non-gravitational analysis on Halley
$0.6^{+0.9}_{-0.4}$	Sagdeev *et al.* 1988	H_2O outgassing and non-gravitational analysis on Halley
<0.7–1.5	Boss 1994	SL9 theoretical models of tidal disruption
0.5	Asphaug & Benz 1994	SL9 models of tidal break-up of primordial rubble pile.
<0.4	Samarasinha & Belton 1995	Numerical simulation of comet rotational state evolution

of meters for $r=30$ AU. After decoupling, these cometary building blocks will gravitationally collapse to form bodies $\approx 1-10$ km in size. The building blocks will be porous on small scales, but relatively compact, whereas the final comet nucleus is expected to have voids as a result of low encounter velocities during the gravitational collapse. This type of structure is verified in computer simulations for statistical random packings of spheres (Dodds 1975; Dodds & Kuno 1977) which shows that there can be significant void space even in closely pack spheres, and that rough, irregular shapes will have less packing efficiency. This will create a body which has some strength in its sub-units but which will have an overall low bulk density. Furthermore, during the 10^6 year time scale of formation, cometesimals from a range of distances will come together in a single comet, allowing for inhomogeneities which can be the underlying cause of outbursts.

Although Chiron is certainly not a typical comet, the density inferred from these observations is consistent with the densities being determined for comets P/Halley and comet D/Shoemaker-Levy 9 (shown in Table 6). To date, there has been no direct measurement of a cometary nucleus density; all have been model dependent determinations. As seen from Table 6, there is a wide variation in the estimates for the density of Comet P/Halley; however, the models of Samarasinha & Belton (1995) are the only ones to utilize a correct spin model for the nucleus and nongravitational reaction forces. This shows that at least for 2 comets, the probable bulk nucleus density is much less than 10^3 kg m^{-3}.

5.3 Other Observations

Finally, it is important to take into consideration other Chiron observations, to assure that the conclusions we have drawn from the present *HST*/ground-based observations are consistent with these observations. A straight comparison between previous observations and the bound coma model for Chiron is difficult because published relative fluxes have not consistently referred to the same quantities. Therefore in Table 7 we present the tabulation of these various properties based on the best-fit model parameters from the *HST* observations along with the observed ground-based constraints. Equations (5) are used to compute the relative fluxes

$$F_{Nuc} = B_{Nuc} + \pi S B_{inner} p_{Nuc}^{(\alpha_1+2)}/(\alpha_1+2),$$
$$F_{inner} = B_{Nuc} + \pi S B_{inner}[2R_e^{(\alpha_1+2)} - p_{Nuc}^{(\alpha_1+2)}]/(\alpha_1+2), \quad (13)$$
$$F_{outer} = F_{inner} + 2\pi S B_{outer}[p_{outer}^{(\alpha_2+2)} - R_e^{(\alpha_2+2)}]/(\alpha_2+2),$$

where F_{Nuc} is the total flux for $p<p_{Nuc}$, F_{inner} is the total flux for $p<R_e$, F_{outer} is the total flux for $p<p_{outer}$, and

$$B_{Nuc} = 10^{-0.4m_\odot}[p_\lambda R_N^2/(2.235\times 10^{22} r^2 \Delta^2)], \quad (14)$$

where $m_\odot$ is the apparent magnitude of the sun, p_λ is the geometric albedo (assumed to be $p_v = 0.11 \pm 0.01$ after Lebofsky *et al.* 1984) of the nucleus at the wavelength of the observation, λ and r and Δ are the heliocentric and geocentric distances in AU. Calculations were done for a range of aperture sizes, p_{outer}, but only the results for $p_{outer}=5''$ are presented in Table 7. In these computations, the total mag-

TABLE 7. Chiron relative flux comparisons.

		Calculated Parameters								Observed Constraints		
Ref	Date	f_{Nuc}	f [5″]	f_b	f_{nc} [5″]	α_1	α_2	Δm_c [mag]	Δm_o [mag]	m_R	α_2	Other
1	2/89	0.76	0.47	0.15	0.89	−1.0	−2.1	0.04	0.05	16.13	−2.1	$f=0.55$
2	4/89	0.66	0.41	0.21	0.70	−1.0	−2.4	0.04		16.39	−2.6	$f_{nc}=0.8$
3	9/89	0.75	0.44	0.15	0.77	−1.7	−1.5	0.04	0.04	16.43	−1.5	
2	12/89	0.76	0.53	0.16	1.14	−1.6	−2.3	0.05		16.08	−2.6	$f_{nc}=1.21$
3	1/90	0.79	0.53	0.14	1.13	−1.0	−2.2	0.05	0.04	16.18	−2.2	$f_b=0.1$–0.2
4	2/93	0.87	0.86	0.13	6.06	−1.7	−3.5	0.08	≈0.02	15.97	−3.5	

Notes to TABLE 7.

f is the fractional flux that the nucleus contributes to the total brightness within a 5″ radius aperture; f_b is the fractional flux that the bound coma contributes to the total brightness; f_{nc} is the ratio of the nucleus flux to the coma flux; Δm_c and Δm_o are the calculated and observed rotational lightcurve ranges for a 5″ radius observing aperture. References: [1]West (1991); [2]Meech & Belton (1990); [3]Luu & Jewitt (1990); [4]This paper.

nitude within a 5″ radius aperture was required to match the observed m(5″). In addition, the calculations held the observed slope of the surface brightness profile for the outer coma, α_2, fixed. The values of f_{Nuc} and α_1 were adjusted so that the "other constraints" listed in Table 7 were met. Finally, the expected rotational lightcurve range, Δm was calculated for the relative coma contribution for comparison with the observed ranges. The reduced lightcurve range is given by

$$\Delta m = -2.5\log[(B_{Nuc}(\min)+B_{coma}(p))/(B_{Nuc}(\max)+B_{coma}(p))]. \quad (15)$$

By using

$$\varepsilon = B_{Nuc}(\min)/B_{Nuc}(\max) = 10^{-0.4\Delta m_0}, \quad (16)$$

we can express Δm in Eq. (15) in terms of the observed bare nucleus range, Δm_0 (c.f. Meech *et al.* 1993a):

$$\Delta m = -2.5\log\left[\frac{2/(1+\varepsilon)B_{Nuc}+B_{coma}(p)}{2\varepsilon/(1+\varepsilon)B_{Nuc}+B_{coma}(p)}\right], \quad (17)$$

where $B_{coma}(p)$ is the $F_{outer}-B_{Nuc}$ as determined from Eq. (13) for a particular observing aperture radius, p.

Inspection of Table 7 shows that for all of the data sets for which there is sufficient information for comparison, there is excellent agreement between the calculated relative fluxes and observed constraints using the 2-component coma model. From the table it is clear that f_{Nuc} remains relatively high, and that the bound portion of the coma makes a 10-20% contribution to the total coma brightness. The relative effect on Chiron's total light curve behavior, however, depends on the ratio of total flux from the nucleus relative to the coma, f_{nc}. At the time of Chiron's greatest intrinsic brightness, near $r=12$ AU, the coma contributed roughly 64% of the total observed flux, of which nearly 25% of this was due to the bound coma. While the contribution from the bound coma have never been the dominant contribution to the total flux from Chiron, the bound coma clearly is an important photometric component even though it is not directly resolvable from the ground.

The parameters α_1 and α_2, which represent the steepness of the inner and outer coma surface brightness profiles, change significantly with time. It is possible that this reflects both differences in activity levels as well as in the scattering properties of the escaping dust grains. The calculated rotational lightcurve ranges are in agreement with the observations with the exception of the 2/93 data where the observed range near $\Delta m=0.02$ mag is considerably smaller than the predicted range $\Delta m=0.08$ mag. The calculations of the decrease in range with increase in relative coma contribution to the total flux assumes that the lightcurve variations are based on Chiron's shape. The observations from 2/93 were made as the total absolute brightness of Chiron had been diminishing since its peak near $r=12$ AU. In the presence of a bound atmosphere, where many of the particles will eventually impact with the surface, it is likely that there would be a redistribution of albedo features on the surface, and it may be expected that a relatively uniform albedo layer would be deposited on the surface which would damp out an albedo related rotational lightcurve variation.

The present dataset is too limited in scope to resolve all the complex issues arising with the dynamics of the particles in Chiron's coma, specifically the balance between the escaping grains (including knowledge of the size distribution) and those which re-impact onto Chiron's surface. Additionally, the present data is not of sufficient signal to noise to directly examine the inner coma for variability in extent and structure with time. However, we have obtained cycle 5 *HST* time with the Faint Object Camera in order to obtain high resolution images of Chiron at 3 dates near perihelion and Earth close approach, and coupled with extensive ground-based observations and modelling the next data set should be able to resolve these issues and place much stronger constraints on the density of Chiron.

The occultation of Chiron on 1993 November 7, reported by Bus *et al.* (1996) showed both a clear chord across the nucleus, as well as several possible features in the coma. The most prominent of these features is a broad asymmetric dust component centered around the time of the central nucleus occultation. The authors conclude that there is no evidence for an exopause boundary or bound material in quasi-stable orbits around Chiron. For the 1993 February data, the models described above imply that the surface brightness of the dust coma within the 2.5×2.5″ square pixels used by Bus *et al.* (1996) at the distance of the exopause, $R_e=1800$ km, would have been roughly a factor of 40 less than the brightness of the nucleus. Given the signal to noise of the occultation data, it is not clear that the change in coma slope indicative of the exopause boundary could have been detected. At least in the 1993 February ground-based data there was considerable asymmetry in the outer coma—which is similar to what was seen in the occultation data. It is not clear that this data could resolve the issue of an exopause.

Finally, we consider the possibility (Jewitt, private communication) that the observed near-nucleus material does not represent a bound coma, rather a "shell" of material from a variable source function, or that the coma represented a halo of very volatile grains which were sublimating and disappearing as they moved away from the nucleus. Given that the observed extended structure remained more or less constant over the 3 weeks between sets of *HST* observations, it is unlikely that this represents an expanding shell of material from variable activity. As noted above in Sec. *5.1*, laboratory experiments show that highly volatile ices trapped in water ice when sublimating preferentially eject grains composed of water ice and refractory material, not grains of more volatile ices. At these heliocentric distances, grain lifetimes are measured in years (Hanner 1981) for water-ice grains, thus a boundary created by sublimating grains does not seem likely as an alternate explanation for the bound coma.

6. CONCLUSIONS

The near-simultaneous *HST* and ground-based observations obtained during 1993 February have provided the first high resolution look at the near-nucleus regions of Chiron for which we hypothesized that the large nucleus mass should have a much larger gravitational influence on the coma struc-

ture than is typical for comets. Specifically, we conclude that:

• After careful deconvolution of the *HST* data, and comparison with extensive simulations, we conclude that there is extended structure seen in the near-nucleus regions (out to 0.3″) around Chiron.

• Near simultaneous ground-based measurements show a faint coma extending out to a projected distance of 9×10^4 km near a position angle of 315°. The outer coma had a steep surface brightness profile, with a slope of -3.1 from 1–3.3″ and -2.2 from 3.3–9.8″.

• Comparison with a simple heuristic model of Chiron, suggests that this structure can best be interpreted as the signature of the exopause boundary at a projected distance of 1800 km from the center of Chiron's nucleus. The simulations which best match the *HST* and ground-based observations assumed a 90 km radius nucleus which contributed $f_{Nuc}=0.8$ of the flux within the bound coma, an inner surface brightness gradient of -1.7 and a gradient near -3.5 outside the bound coma. The parameter, f_{Nuc}, is in agreement with inferred values of f_{Nuc} from ground-based observations from 1989 through 1993. Single component models could only match the *HST* observations using an unrealistically low value of $f=0.1$, which is inconsistent with ground-based data and would imply that the nucleus flux contribution was insignificant compared to that of the coma.

• Utilizing ground-based measurements of the grain reflectivity we find that for grains in Chiron's outer coma neutral scattering occurs at smaller grain sizes than is typical for most comets, i.e., near $\lambda=0.6$ μm. Combining this with estimates of cometary grain densities, we infer from the extent of the bound coma that Chiron's nucleus density should be less than 10^3 kg m^{-3}.

The image processing in this paper has been performed in part by using the IRAF program. IRAF is distributed by the National Optical Astronomy Observatories, which is operated by the Association of Universities for Research in Astronomy, Inc. (AURA) under cooperative agreement with the National Science Foundation. We are particularly grateful to T. Lauer for introducing us to the CLEAN algorithms and to J. Holtzman for useful discussions about deconvolution techniques. We would also like to thank H. Weaver and O. Hainaut for their helpful comments and Lucy deconvolution tests. Support for this work was provided by NASA through grant number GO.3769.01-91A from the Space Telescope Science Institute, which is operated by the Association of Universities for Research in Astronomy, Incorporated, under NASA contract NAS5-26555. Additional support for this work was provided by NASA Grant No. NAGW-1897 [kjm].

REFERENCES

Asphaug, E., & Benz, W. 1994, Nat, 370, 120
Banaszkiewicz, M., & Ip, W.-H. 1991, Icarus, 90, 237
Bar-Nun, A., Herman, G., Laufer, D., & Rappaport, M. L. 1985, Icarus, 63, 317
Bar-Nun, A., & Kleinfeld, I. 1989, Icarus, 80, 243
Boehnhardt, H., & Fechtig, H. 1987, A&A, 187, 824
Boss, A. P. 1994, Icarus, 107, 422
Bradley, J. P., & Brownlee, D. E. 1986, Sci, 231, 1542
Bradley, J. P., Sandford, S. A., & Walker, R. M. 1988, in Meteorites and the Early Solar System, edited by J. F. Kerridge and M. S. Matthews (University of Arizona Press, Tucson) p. 861
Brooke, T. Y., Knacke, R. F., & Joyce, R. R. 1987, A&A, 187, 621
Brownlee, D. E., Pilachowski, L., Olszewski, E., & Hodge, P. W. 1980, in Solid Particles in the Solar System, IAU Symposium 90, edited by I. Halliday and B. A. McIntosh (Reidel, Dordrecht), p. 333
Buie, M. W., & Bus, S. J. 1992, Icarus, 100, 288
Buie, M. W., *et al.* 1993, IAU Circ. No. 5898
Buie, M. W., & Tholen, D. J. 1996, Icarus (in press)
Burns, J. A., Lamy, P. L., & Soter, S. 1979, Icarus, 40, 1
Burrows, C., Holtzman, J. A., Faber, S. M., Bely, P., Husan, H., Lynds, C. R., & Schroeder, D. 1991, ApJ, 369, L21
Bus, S. J., Bowell, E., Harris, A. W., & Hewitt, A. V. 1989, Icarus, 77, 223
Bus, S. J., Bowell, E., Stern, S. A., & A'Hearn, M. 1991, Asteroids, Comets, Meteors IV, 34
Bus, S. J., *et al.* 1996, Icarus, 123, 478
Campins, H., Telesco, C., Osip, D., Rieke, G., Rieke, M., & Schulz, B. 1994, AJ, 108, 2318
Dodds, J. A. 1975, Nat, 256, 187
Dodds, J. A., & Kuno, H. 1977, Nat, 266, 614
Donn, B., & Hughes, D. 1986, in Proceedings of the 20th ESLAB Symposium on the Exploration of Halleys Comet, edited by B. Battrick, E. J. Rolfe, and R. Reinhard, Vol. III (European Space Agency, Paris), p. 523
Donn, B., & Meakin, P. 1987, BAAS, 19, 847
Elliot, J. L., *et al.* 1995, Nat, 373, 46
Gehrz, R. D., & Hanner, M. S. 1988, in Infrared Observations of Comets Halley & Wilson and the Properties of the Grains, report of a Workshop held at Cornell University, edited by M. S. Hanner, p. 50
Green, J. R. 1989, Ph. D. dissertation, University of Texas, Austin
Hanner, M. 1981, Icarus, 47, 342
Hanner, M. 1988, in Infrared Observations of Comets Halley & Wilson and the Properties of the Grains, report of a Workshop held at Cornell University, edited by M. S. Hanner, p. 22
Harris, H. C., Baum, W. A., Hunter, D. A., & Kreidl, T. J. 1991, AJ, 101, 677
Hartmann, W. D., Tholen, D. J., Meech, K. J., & Cruikshank, D. P. 1990, Icarus, 83, 1
Högbom, J. A. 1974, A&AS, 15, 417
Hughes, D. W. 1991, in Comets in the Post-Halley Era, edited by R. Newburn, M. Neugebauer, and J. Rahe (Kluwer, Dordrecht), p. 825
Jewitt, D., & Luu, J. 1992, AJ, 104, 398
Jewitt, D., & Meech, K. J. 1986, ApJ, 310, 937
Keel, W. C. 1991, PASP, 103, 723
Khare, B. N., Arakawa, E. T., Thompson, W. R., & Sagan, C. 1987, BAAS, 19, 895
King, I. R., *et al.* 1991, AJ, 102, 1553
Kissel, J., *et al.* 1986, Nat, 321, 336
Krasnopolsky, V. A., *et al.* 1987, A&A, 187, 707
Lamy, P. L., Grün, E., & Perrin, J. M. 1987, A&A, 187, 767
Lamy, P. L., Malburet, P., Llebaria, A., & Koutchmy, S. 1989, A&A, 222, 316
Lamy, P. L., & Perrin, J. M. 1980, in Solid Particles in the Solar System, IAU Symposium 90, edited by I. Halliday and B. A. McIntosh (Reidel, Dordrecht), p. 75
Landolt, A. U. 1983, AJ, 88, 439
Landolt, A. U. 1992, AJ, 104, 340
Lauer, T. R., *et al.* 1992a, AJ, 103, 703
Lauer, T. R., *et al.* 1992b, AJ, 104, 552
Lebofsky, L. A., Tholen, D. J., Rieke, G. H., & Lebofsky, M. J. 1984, Icarus, 60, 532
Luu, J. X., & Jewitt, D. C. 1990, AJ, 100, 913

Meech, K. J., & Belton, M. J. S. 1990, AJ, 100, 1323
Meech, K. J., Belton, M. J. S., Mueller, B. E. A., Dickson, M. W., & Li, H. R. 1993a, AJ, 106, 1222
Meech, K. J., Buie, M. W., Mueller, B. E. A., & Belton, M. J. S. 1993b, BAAS, 25, 1057
Mendis, D. A., Houpis, H. L. F., & Marconi, M. L. 1985, Fund. Cosmic Phys., 10, 1
Möhlmann, D. 1995, Planet. Space Sci. , 43, 327
Mukai, T., Mukai, S., & Kikuchi, S. 1987, A&A, 187, 650
Murnaghan, F. D. 1967, Finite Deformation of An Elastic Solid (Dover, New York)
Pailer, N., & Grün, E. 1980, in Solid Particles in the Solar System, IAU Symposium 90, edited by I. Halliday and B. A. McIntosh (Reidel, Dordrecht), p. 365
Peale, S. J. 1989, Icarus, 82, 36
Rickman, H. 1989, Adv. Space Res., 9, 59
Ritchie, C. E, & MacKenty, J. W. 1993, in Selected WF/PC Instrument Science Reports and Memos, edited by J. W. MacKenty *et al.*, STScI, WF/PC Instrument Science Report 93-02
Sagdeev, R. Z., Elyasberg, P. E., & Moroz, V. I. 1988, Nat, 331, 240
Samarasinha, N. H., & Belton, M. J. S. 1995, Icarus, 120, 443
Schwarz, U. J. 1978, A&A, 65, 345
Sekanina, Z. 1982, AJ, 87, 1059
Sekanina, Z. 1983, AJ, 88, 1382
Sekanina, Z. 1985, AJ, 90, 827
Shaw, R. A., & Horne, K. 1992, in Astronomical Data Analysis Software and Systems I, PASP Conf. Ser. 25, edited by E. M. Worrall, C. Biedmesderfer, and J. Barnes, p. 311
Smirnov, V. N., Vaisberg, O. L., & Anisimov, S. 1987, A&A, 187, 774
Sparks, W. B., Ritchie, C., & MacKenty, J. 1993, in Selected WF/PC Instrument Science Reports and Memos, edited by J. W. MacKenty *et al.*, STScI, WF/PC Instrument Science Report 92-09
Spencer, J. R., Lebofsky, L. A., & Sykes, M. V. 1989, Icarus, 78, 337
Stern, S. A., Jackson, A. A., & Boice, D. C. 1993, AJ, 107, 765
Sykes, M. V., & Walker, R. G. 1991, Sci, 251, 777
Tan, S. M. 1986, MNRAS, 220, 971
Tanaka, H., & Ida, S. 1996, Icarus, 120, 371
Walker, R. M. 1988, in Infrared Observations of Comets Halley & Wilson and the Properties of the Grains, report of a Workshop held at Cornell University, edited by M. S. Hanner, p. 53
Wasson, J. T. 1974, Meteorites (Springer, Berlin)
Weidenschilling, S. J. 1994, Nat, 368, 721
Weiss-Wrana, K. 1983, A&A, 126, 240
Weissman, P. 1986, Nat, 320, 242
West, R. M. 1991, A&A, 241, 635